



## Insight into electrochemical passivation behavior and surface chemistry of 2205 duplex stainless steel: effect of tensile elastic stress

Longjun Chen, Wei Liu\*, Baojun Dong, Yonggang Zhao, Tianyi Zhang, Yueming Fan, Weijian Yang

*Corrosion and Protection Center, Institute for Advanced Materials and Technology, University of Science and Technology Beijing, Beijing 100083, P. R. China*



### ARTICLE INFO

**Keywords:**  
2205 duplex stainless steel  
Tensile elastic stress  
Passive film  
Electronic characterization

### ABSTRACT

The effect of tensile elastic stress on passivation behavior and surface chemistry of 2205 duplex stainless steel is investigated. Elastic stress increases the potential drop at the film/solution interface, donor density and defects diffusion coefficient, resulting in the increase of passive current density. High elastic stress ( $\geq 60\%\sigma_s$ ) leads to the generation of soluble  $\text{CrO}_3$ , the increase of oxidized Cr and Fe(II) content and the decrease of film thickness, resulting in the quasi-steady-state current density no longer independent of potential. Passive film become denser from spontaneous passivation to primary passivation and Fe(III) compounds dominate the passive film under secondary passivation.

### 1. Introduction

Duplex stainless steel (DSS), such as 2205 type, is increasingly employed as structural materials in a wide range of applications, including oil and gas engineering, marine engineering, and nuclear engineering, due to their superior mechanical properties, economic advantages and corrosion resistance [1–3]. The outstanding corrosion resistance of duplex stainless steel is markedly attributed to the composition, structure, thickness and electronic properties of passive film formed on the surface [4–8]. Nevertheless, when DSS is subjected to harsh environment, the passive film is susceptible to be degraded or penetrated, then resulting in the rapid corrosion and damage of the structure.

Actually, the metallic materials in industries are always used under stressed conditions during service, so investigating the effect of stress (one of environmental factors) on the passivation behavior is very meaningful. Previous extensive studies have demonstrated that the application of tensile stress could increase the pitting and stress corrosion crack (SCC) susceptibility owing to its effect on the mechanical integrity of the brittle passive film [9–12]. Martin et al. [9] reported that metastable pits nucleated on surface near the yield stress ( $\sigma_s$ ), and then oxygen vacancies and the oxygen diffusion increased after reaching  $\sigma_s$  due to the activation of dislocations dynamics, and producing stable pits. Örnek and Engelberg [10] found that the application of 0.2% tensile strain was enough to induce SCC for 2205 DSS after 368 days of

exposure at 30% RH /50 °C with 1450  $\mu\text{m}/\text{cm}^2$  chloride. Hou et al. [12] suggested that sever plastic strain and stress could result in the decrease of critical pitting temperature and pitting potential owing to high initiation frequency and growth rate of metastable pits. Most of these studies were carried out at high stress levels which could introduce plastic deformation, and the effect of stress was thus explained by the brittle mechanical fracture of passive film or dislocation exposed on the surface.

Since elastic stress is the most common in the actual service condition, investigations for the effect of external stress below the yield stress on passive film are also very necessary and meaningful. Unlike plastic stress, elastic stress is less likely to cause the rupture of passive film, but it can still accelerate the corrosion susceptibility. Feng et al. [13,14] believed that the lattice was distorted and the strain energy density increased for the samples subjected to elastic stress, hence the anodic current density increased. Moreover, Zhu and Luo [15] stated that both tensile stress and compressive stress enhanced the surface activity of Alloy 800 in a ferrocenemethanol solution containing potassium chloride and thiosulfate. The elastic stress can not only change the surface state, but also the electronic properties of passive film. Wang et al. [16] indicated that the elastic stress could accelerate the critical current density, passive current density and donor density of the passive film because the applied stress affected the diffusion coefficient for the vacancy type self-diffusion based on the thermodynamic analysis. Vignal et al. [17] found that the electronic properties were significantly

\* Corresponding author.

E-mail address: [weiliu@ustb.edu.cn](mailto:weiliu@ustb.edu.cn) (W. Liu).

modified by the elastic stress, and the passive film was heavily doped and the differential capacitance decreased notably when the applied stress was above 70% $\sigma_s$ . Besides, the transport of oxygen vacancies was also accelerated when an elastic stress was subjected [18]. Unfortunately, a large number of works have been focusing on passive film of alloys, but the electronic characterization of that film on stainless steel are still somewhat limited. Consequently, the study of the composition, microstructure, charge carrier concentrations, point defect densities of passive film and corrosion behavior of DSS is important, especially for the effect of elastic stress.

In this paper, the aim is to deeply and systematically reveal the effect of tensile elastic stress on the electrochemical passivation behavior and surface chemistry of 2205 DSS. The passive film growth/dissolution kinetics, charge carrier density, diffusion coefficient and passive film properties are analyzed using electrochemical techniques, electron backscatter diffraction (EBSD) and X-ray photoelectron spectroscopy (XPS). The effect of passive state (spontaneous, primary and secondary passive) on the film properties is also investigated.

## 2. Experimental

### 2.1. Materials and solutions

The commercial 2205 DSS is employed in this paper, supplied by *JiuGang Group*, with the following chemical composition (wt%): C 0.019, Si 0.540, Mn 1.250, P 0.026, S 0.001, Ni 5.150, Cr 22.470, Mo 3.060, N 0.168, with Fe making up the balance. The material is solution-annealed at 1050 °C for 1 h and then quickly water-cooled by the manufacturer. The mechanical properties including yield strength ( $\sigma_y$ , 0.2% offset), tensile strength ( $\sigma_b$ ), elastic modulus and elongation are 548 MPa, 846 MPa, 200 GPa and 28.0%, respectively. The samples are machined into 70 × 10 × 1 mm. Prior to experiments, specimens are grounded sequentially using up to 5000 grit silicon paper, degreased in an ultrasonic bath with isopropanol, rinsed in ethanol, dried in nitrogen and coated with silicone rubber leaving 1 cm<sup>2</sup> exposed surface at the middle site of steel, as shown in Fig. 1.

To simulate the service environment of 2205 DSS in the production well of an oilfield in China, the simulated produced water is used in this paper. The chemical composition (mg/L) of the test solution is consisted of MgCl<sub>2</sub>·6H<sub>2</sub>O 7329.1, CaCl<sub>2</sub> 3011.6, NaHCO<sub>3</sub> 764.8, Na<sub>2</sub>SO<sub>4</sub> 3001.9, KCl 1416.5 and NaCl 21877.8, with pH 7.66 ± 0.20 at 25 °C, prepared by analytical grade reagent and deionized water (18.25 MΩ·cm). The experimental temperature is maintained at 25 °C during the

measurement.

### 2.2. Four-point bending loaded specimen preparation

Before immersed in the solution, specimens are loaded by Four-point bending setup as shown in Fig. 1. The rotation of the bolt controls the magnitude of surface stress applied to specimens. Based on the below equation, the surface stress can be calculated [19]:

$$\sigma = \frac{12Ety}{3H^2 - 4J^2} \quad (1)$$

where  $\sigma$  is the loading surface stress for the mid-portion of the specimen,  $E$  is the elastic modulus (200 GPa),  $t$  is the thickness of specimen (1 mm),  $y$  is the deflection (mm),  $H$  is the distance between outer supports (60 mm) and  $J$  is the distance between inner and outer supports (15 mm). The specimens are applied with a constant tensile stress at 0%, 30%, 60% and 90% of its yield strength, i.e., 0 MPa, 164.4 MPa, 328.8 MPa and 493.2 MPa, respectively. After loading at the designed value for 10 min, the stressed sample is immersed into the electrolyte for the subsequent electrochemical measurements.

### 2.3. Electrochemical measurement

Electrochemical measurements are performed with a Gamry interface 1010E electrochemical workstation in a classical three-electrode cell, a platinum sheet and Ag/AgCl KCl saturated electrode act as counter electrode and reference electrode, respectively. Before experiments, the working electrode is initially potentiostatically polarized at −1.0 V vs. Ag/AgCl (all potential versus Ag/AgCl in this paper) for 10 min to remove passive film formed in air. After measuring the open circuit potential (OCP) for 1 h, cyclic potentiodynamic polarization tests are started from −0.5 V to the potential corresponding to the anodic current density value of 1 mA/cm<sup>2</sup> and then reversed back to the initial potential with a scan rate of 1 mV/s. Potentiostatic polarization tests are performed at the designed potential for 1 h and the quasi-steady-state current density ( $I_{ss}$ ) for each current-time curve is calculated from the average value of the last 10 s. Electrochemical impedance spectroscopy (EIS) tests are conducted at OCP or the designed anodic potential using an oscillating potential ± 5 mV in the frequency range from 100 kHz to 10 mHz with 10 points per decade after passive film formed at the designed potential for 1 h. Mott-Schottky curves of spontaneous passive sample are performed by sweeping the potential from −0.70–1.30 V at

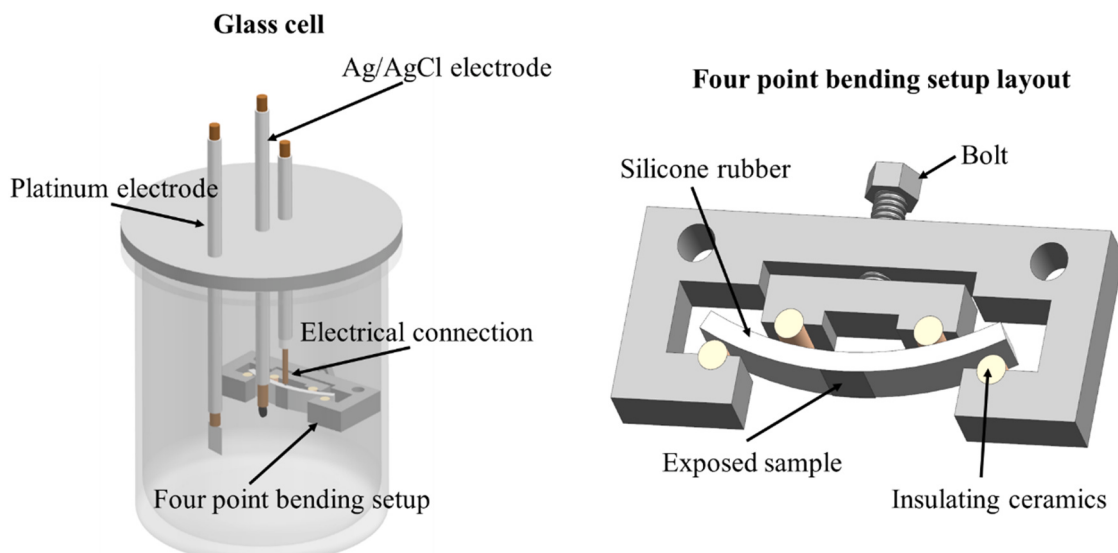


**Fig. 1.** Schematic diagram of the experimental setup.

1 kHz using an oscillating potential  $\pm 10$  mV with a step rate of 25 mV/s. For the primary passive sample, Mott-Schottky measurements are swept from the designed anodic potential to the cathodic direction. All the electrochemical measurements are repeated at least three times to verify the reproducibility and the typical results are chosen to present.

#### 2.4. Surface characterization

Grain boundary information and local misorientation (LMO) are characterized by Electron backscatter diffraction (EBSD) experiments using an EBSD system attached to a JSM-6301 field emission gun scanning electron microscopy. X-ray photoelectron spectroscopy (XPS) is preformed to examine the chemical composition of passive film formed on specimens using Thermo Scientific K-Alpha. The XPS depth profiles are obtained by  $\text{Ar}^+$  ion bombardment with an ion beam of 1 kV, and the sputtering rate, as calibrated on a thermally oxidized  $\text{SiO}_2/\text{Si}$ , is approximately 0.1 nm/s. All XPS peaks are corrected to the standard carbon C 1 s binding energy, 284.8 eV. At the end of the experiment, the sample is immediately destressed, rinsed in ethanol, dried in nitrogen, vacuum packed and XPS tested within 8 h to reduce the effect of oxygen contamination.

### 3. Results

#### 3.1. Microstructure analysis

The detailed information on the microstructures of 2205 DSS under  $0\%\sigma_s$ ,  $60\%\sigma_s$  and  $90\%\sigma_s$  by EBSD analysis are shown in Fig. 2. As observed in Fig. 2(a), (d) and (g), all three samples present a few

annealing twins in austenite phase, this is due to the low stacking energy of 2205 DSS. In phase maps, the red and green areas represent the ferrite ( $\alpha$ ) and austenite ( $\gamma$ ), respectively. For all three samples, the austenite ( $\gamma$ ) grains are arrayed in island like structure and embedded in the ferritic ( $\alpha$ ) matrix, and the diameter of austenite ( $\gamma$ ) grains are generally larger than that of ferritic ( $\alpha$ ) matrix, as shown in Fig. 2(b), (e) and (h). Moreover, there is no notable change in grain size and shape induced by stress. These indicate that  $60\%\sigma_s$  and  $90\%\sigma_s$  cannot change the basic microstructure. There is no obvious change in the high-angle grain boundaries (HAGB,  $> 15^\circ$  of misorientation, represented by thin blue lines) for three samples. But the low-angle grain boundaries (LAGB, between  $2^\circ$  and  $15^\circ$  of misorientation, represented by thin red lines) length slightly climbs from 1.16 mm to 1.25 mm as the stress increases from 0% to  $60\%\sigma_s$ , and it further increases to 1.54 mm by  $90\%\sigma_s$  stress, as presented in Fig. 2(c), (f) and (i). Such increase suggests the strain moderately accumulated when the sample is subjected to  $90\%\sigma_s$ . Meanwhile, the fraction of  $\Sigma 3$  twin boundaries (represented by thick green lines) has been slightly decreased by stress.

Fig. 3 shows kernel average misorientation (KAM) analysis of samples under  $0\%\sigma_s$ ,  $60\%\sigma_s$  and  $90\%\sigma_s$ . In terms of  $60\%\sigma_s$  sample, the kernel misorientation distribution is similar to that of  $0\%\sigma_s$  sample. For sample with  $90\%\sigma_s$  stress, the KAM presents a broader distribution and a higher misorientation value corresponding to the maximum fraction, as shown in Fig. 3(d), indicating slightly intensified strain in phase. Such increase in KAM degree shows that  $90\%\sigma_s$  stress could induce higher density of dislocations and other defects [20]. These suggest that lattice distorts induced by stress and can enhance the surface activity [13,14]. Moreover, ferrite has slightly less local strain hot spots than austenite for all three samples, and this phenomenon is more remarkable in the  $90\%\sigma_s$

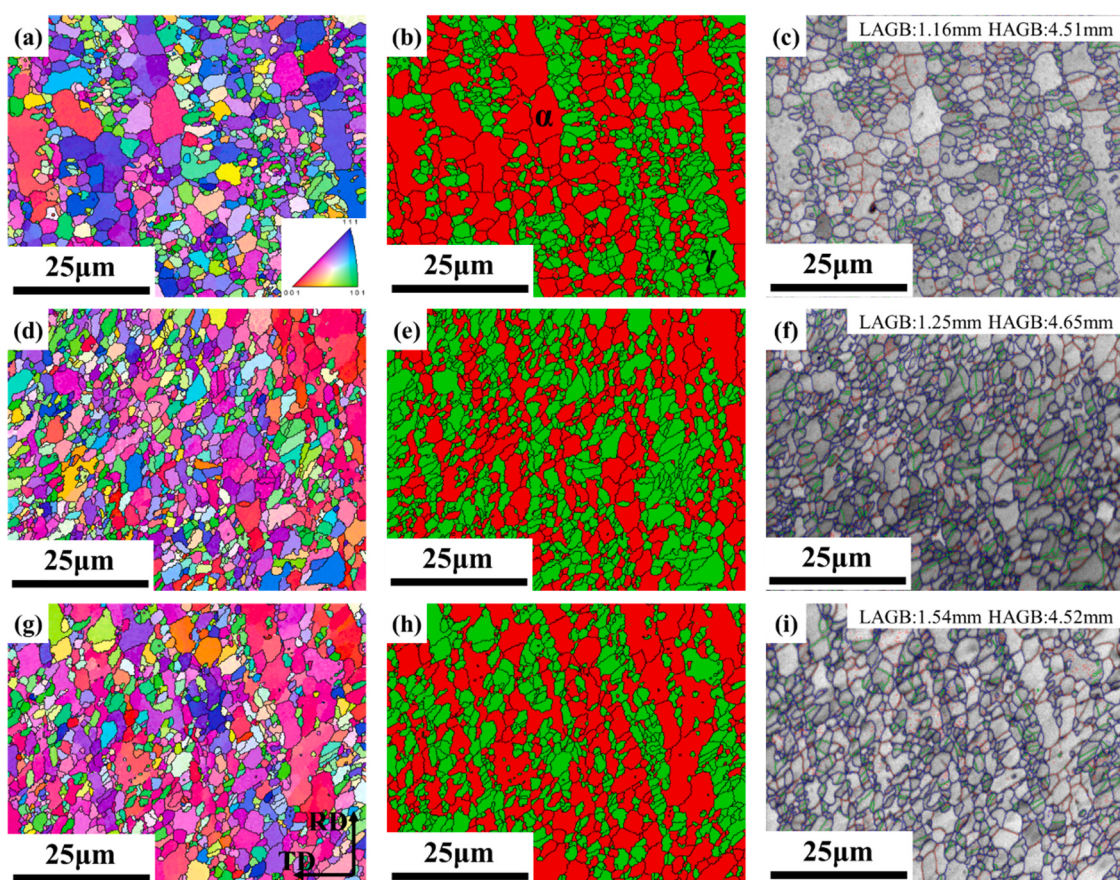


**Fig. 2.** EBSD results of 2205 DSS under  $0\%\sigma_s$  (a, b, c),  $60\%\sigma_s$  (d, e, f) and  $90\%\sigma_s$  (g, h, i): (a, d, g) inverse pole figures, (b, e, h) phase maps (red and green areas represented the ferrite ( $\alpha$ ) and austenite ( $\gamma$ ), respectively), (c, f, i) grain boundary maps with LAGB (thin red lines), HAGB (thin blue lines) and  $\Sigma 3$  twin boundaries (thick green lines).

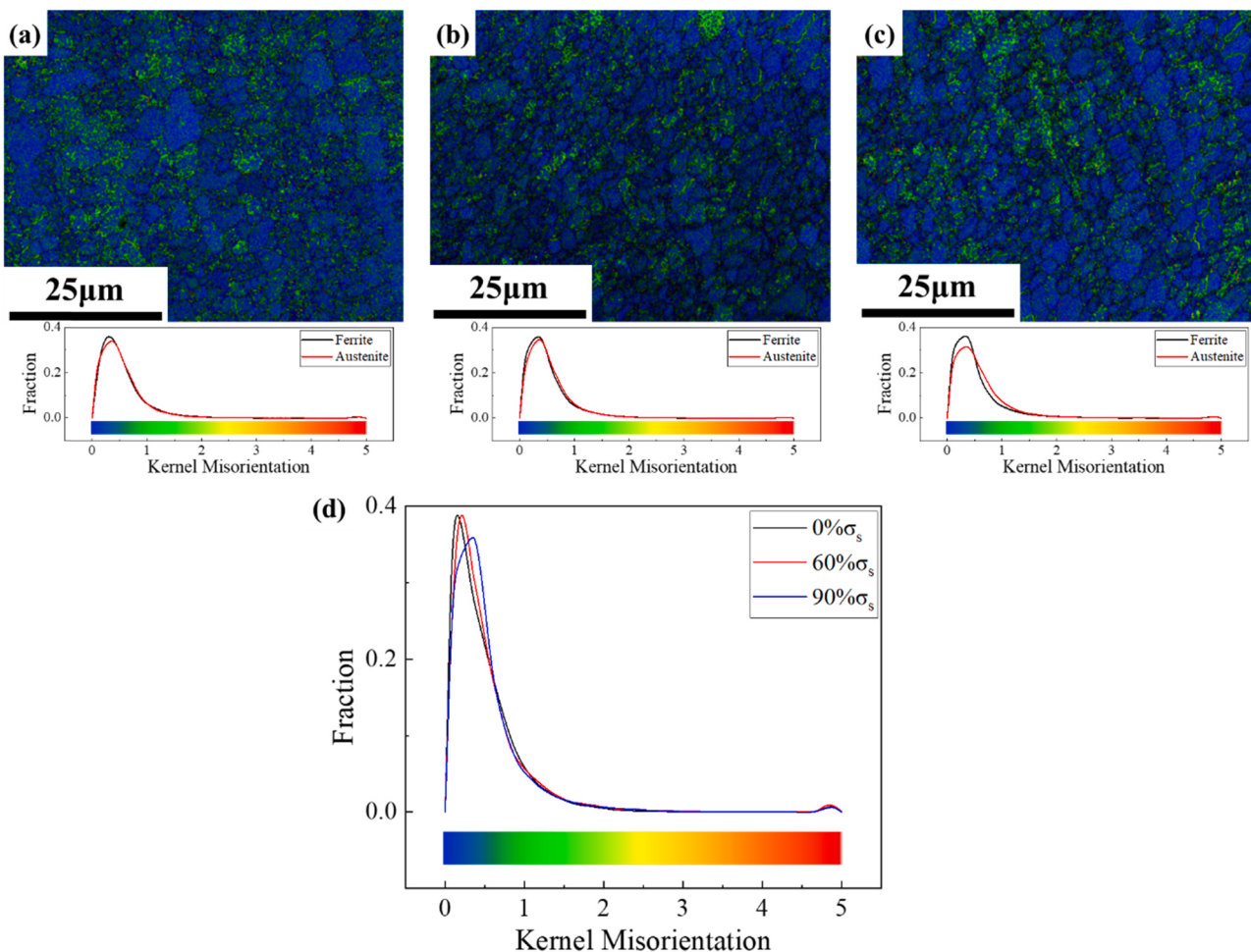


**Fig. 3.** EBSD kernel average misorientation maps of samples under 0% $\sigma_s$  (a), 60% $\sigma_s$  (b) and 90% $\sigma_s$  (c) in Fig. 2 and kernel misorientation distribution (d). Black lines are grain boundaries.

sample. This indicates that strain localization intensifies in austenite grains, and austenite is modestly more deformed than ferrite, but this effect is limited compared with that under plastic stress [10].

### 3.2. Open circuit potential

The typical variation of open circuit potential (OCP) with time of

2205 DSS is presented in Fig. 4. Due to the presence of dissolved oxygen, a spontaneous passive film is formed on the surface when 2205 DSS is immersed in the solution. It is seen that OCP values of 2205 DSS stressed at different levels soar sharply at the very beginning, and then slowly increase with time. Roughly 400 s, the OCP do not change significantly anymore and gradually attain to the quasi-steady-state. No significant differences are detected in OCP value under different stress levels, and

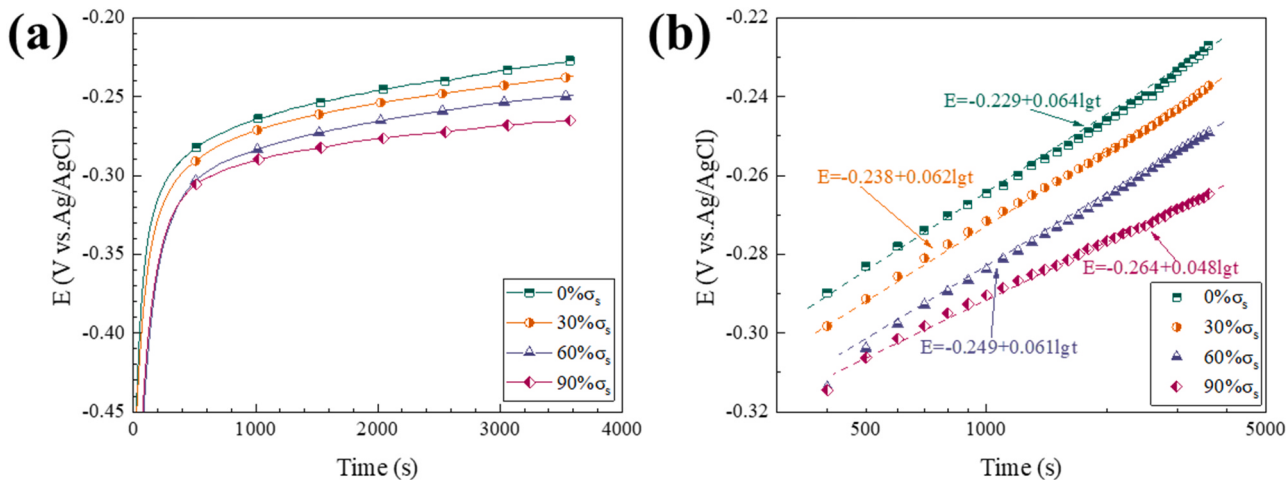


**Fig. 4.** The variation of open circuit potential with time of 2205 DSS applied different levels of stress: (a) linear X-axis; (b) logarithmic X-axis.

all of them are about  $-0.25$  V. However, the OCP locates at a little more negative value for 2205 DSS subjected to  $90\%\sigma_s$ , compared to no stress sample. As Song et al. [21] stated, OCP could reflect the integrity and density of the passive film of stainless steel in the solution, the more positive OCP value, the better passive state of the stainless steel with more compact and denser passive film. Hence, the decrease of OCP is attributed to thinning of the passive film or a less compact passive film formed on the surface. In other words, the passivation state of 2205 DSS becomes modestly worse when stress increases.

Moreover, the relationship between OCP and thickening rate of oxide film is listed as [22,23]:

$$E = \text{const.} + \frac{2.303\delta^- \lg t}{P} \quad (2)$$

where  $E$  is OCP value, const. is a constant depends on the material, the type and concentration of aggressive anions,  $\delta^-$  is the thickening rate of passive film per unit decade of time,  $P$  is a constant ( $39$  nm/V [23]) and  $t$  is time. As presented in Fig. 4(b), OCP is linear with  $\log t$  for all samples, which is in consistent with Eq. (2). As shown, the slopes decrease with the increase of stress, and then the calculated  $\delta^-$  values decrease with the increase of stress, i.e.,  $1.08$ ,  $1.05$ ,  $1.03$  and  $0.81$  nm/unite decade of time for the  $0\%\sigma_s$ ,  $30\%\sigma_s$ ,  $60\%\sigma_s$  and  $90\%\sigma_s$  sample, respectively. The lower  $\delta^-$  value for the sample applied to  $90\%\sigma_s$  implies that stress slows down the formation rate of passive film.

### 3.3. Potentiodynamic and potentiostatic polarization

Fig. 5 shows the typical cyclic potentiodynamic polarization results of 2205 DSS subjected to different stress. In terms of cathodic polarization curves, all curves almost overlap with each other, indicating that stress do not introduce any change to the cathodic process. Moreover, the cathodic Tafel slopes are about  $-110$  mV/decade, and thus the cathodic reaction is dominated by water reduction [24]. Anodic polarization curves show that 2205 DSS could spontaneously passive because no active-passive current plateau in the range of low overpotential is observed. These curves could be divided into four potential regions [25], e.g., for no stress sample,  $-0.25$  V~ $0.50$  V represents primary passive,  $0.5$  V~ $0.8$  V is corresponding to transpassive dissolution due to the dissolution of  $\text{Cr}_2\text{O}_3$  in passive film to  $\text{CrO}_4^{2-}$  [26],  $0.8$  V~ $0.98$  V is related to secondary passive and above  $0.98$  V associates with oxygen evolution and passive breakdown, respectively. With an increase in the stress level, the corrosion potential slightly decreases and the corrosion

current density slightly increases, indicating that the resistance to general corrosion weakens. Furthermore, the right shift of anodic polarization curve illustrates higher passive current density induced by stress. According to the work by Heine et al. [27], the passive current density approximately reflects the dissolution rate of passive film during the passive process. Therefore, a higher passive current density leads to a higher dissolution rate in the passive film, suggesting that the passive film with lower protective ability forms under higher stress.

The typical current-time curves in linear and double logarithmic coordinates of 2205 DSS potentiostatic polarized at  $0.2$  V for  $1$  h are displayed in Fig. 6(a) and (b), respectively. It could be seen that the anodic current density for each condition slumps radically in the initial stage because of the rapid nucleation and growth of passive film [28]. Then the anodic current density decreases sluggishly as time prolonged and gradually maintains at a relatively stable value as shown in inserted image in Fig. 6(a), and this is attributed to the balance of film formation and dissolution [29]. Moreover, no remarkable current peak is observed, indicating that no breakdown events occurs during the formation of stable passive film [28,30]. According to previous work by Jones and Greene [5,31], the relationship between current density  $I$  and time  $t$  can be expressed as  $I = \psi t^{-k}$ , where  $\psi$  is a constant associated with the maximum current density of film-free surface and  $k$  is the passivation index which is deemed as an indirect parameter in characterizing the film properties. As presented in Fig. 6(b), all curves obey the above equation, and value of  $k$  is  $1.096$  for no stress specimen, suggesting a compact and highly protective passive film forms on surface [8]. Furthermore, values of  $k$  reduces with the increment of stress because of film degradation, which agrees with OCP results.

The quasi-steady-state current density as a function of potential within the primary passive range is presented in Fig. 6(c). Many researchers [5,8,30,32] stated that the quasi-steady-state was so difficult to be achieved within short time, and Burstein and Daymond [32] reported the passive current density continued to decrease after  $15$  h. As exhibited in Fig. 6(b), the measured current density of 2205 DSS still persistently slides after polarization for  $1$  h. Whereas, the aim of this study is to unravel the passivation behavior influenced by stress, and thus the quasi-steady-state current density after  $1$  h is used like previous works [5,8,33,34]. The current density at quasi-steady-state ( $I_{ss}$ ) is a constant and independent with potential, i.e.,  $0.225$   $\mu\text{A}/\text{cm}^2$  and  $0.289$   $\mu\text{A}/\text{cm}^2$  for samples with no stress and  $30\%\sigma_s$ , respectively, as presented in Fig. 6(c). According to the point defect model (PDM) [26], a passive film whose charge-transfer properties are controlled by the movement of oxygen vacancies and cation interstitials is predicated to yield a quasi-steady-state current density. However, the current density almost increases linearly with the increase of applied potentials when stress increases to  $60\%\sigma_s$  and  $90\%\sigma_s$ , and the slope, i.e.,  $dI_{ss}/dE$  for sample subjected to  $90\%\sigma_s$  is much larger than that of  $60\%\sigma_s$ . It indicates that the quasi-steady-state current density  $I_{ss}$  is dependent of the formation potential under these two conditions, the similar phenomena are also observed by Li et al. [35] and Kong et al. [36]. This can be attributed to the stress changing the structure of passive film and then enhancing passive film dissolution at high anodic potentials or the oxidation state change of passive film [8, 17, 35, 36].

### 3.4. Electrochemical impedance spectroscopy analysis

In order to further figure out the passive property, three different passive conditions, i.e., spontaneous passivation (OCP), primary passivation (0~ $0.4$  V) and secondary passivation (0.9 V) of 2205 DSS applied to different stress is investigated by EIS after film formation for  $1$  h, as presented in Fig. 7. All the EIS data have been validated by Kramers-Krong (K-K) transforms to access the reliability, and the measured data are consistent with the calculated data. As shown in Nyquist plots, all the spectra are characterized as unfinished semi-arcs, suggesting a similar passive mechanism. Diameters of Nyquist diagrams

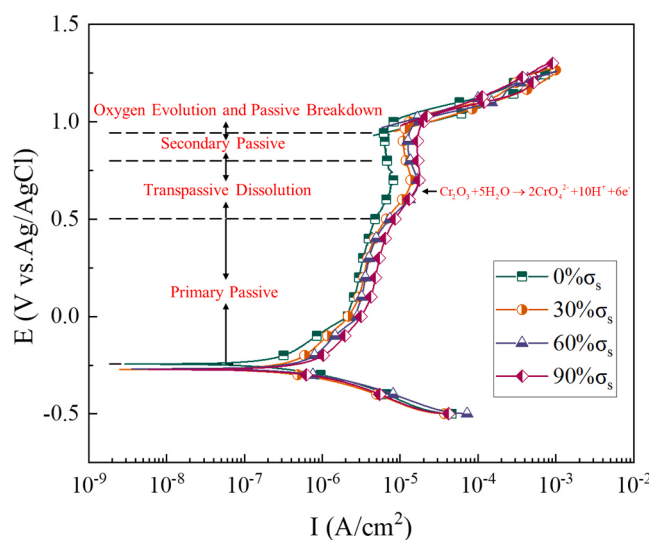
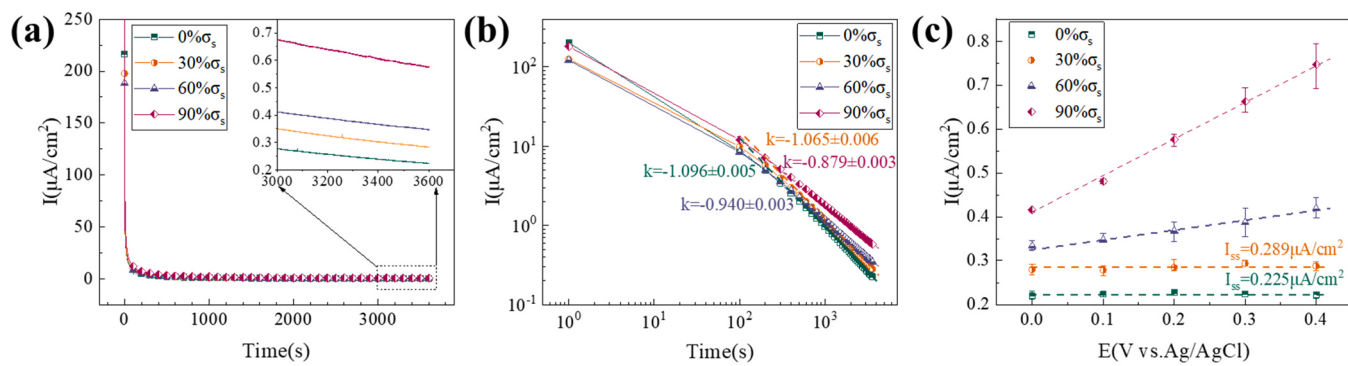


Fig. 5. Cyclic potentiodynamic polarization curves of 2205 DSS applied different levels of stress.



**Fig. 6.** Current-time transients in linear (a) and double logarithmic coordinates (b) at 0.2 V, and quasi steady-state current density as function of potential (c) of 2205 DSS subjected to different stress.

decrease with the increase of stress at a certain potential, indicating that stress weakens the property of passive film but do not change the basic passive mechanism. In the Bode diagrams, the impedance moduli display a relatively linear slope close to  $-1$  and the phase angles evolve between  $-80^\circ$  and  $-60^\circ$  in the medium and low frequency, indicating that the passive film is close to ideal capacitance [34]. For all conditions, the passive film formation potential has a remarkable effect on the EIS. The impedance of the system is relatively small when passive film spontaneously forms, it increases by shifting the potential to primary passive potential region, and then decreases up to the potential where transpassivity occurs, similar results are observed by Cui et al. [5] and Mohammadi et al. [37]. Moreover, the EIS results almost overlap with each other within primary passive potential region especially for the specimen with no stress and 30%σ<sub>s</sub>, and such the lack of sensitivity of impedance to the applied potential proves that the electric field strength in the passive film is imperceptible to the anodic potential [38].

According to Priyantha et al. [39], three time constants are usually used to model EIS for the whole electrode/film/electrolyte system of corrosion-resistant alloy in the passive range:

$$Z_{\text{total}} = Z_{m/f} + Z_f + Z_{e/f} \quad (3)$$

where  $Z_{m/f}$ ,  $Z_f$  and  $Z_{e/f}$  represent the metal/film interface impedance, the film impedance and the electrolyte/film interface impedance, respectively. However, not every time constant can be observed for all conditions due to the different electrochemical system or overlapping of time constants. Based on the above results, the simple Randle circuit  $R_s(Q_fR_f)$  as inserted in Fig. 7(a) is employed to analyze the EIS data of 2205 DSS. The variable  $Q_f$  (CPE, constant phase element) is employed to signify the non-ideal capacitance, which is caused by an inhomogeneous current flow. In this circuit,  $R_s$  is solution resistance,  $Q_f$  and  $R_f$  are the constant phase element and resistance of the passive film, respectively. The typical fitted results are listed in Table 1. As shown,  $n$  (dispersion coefficient of  $Q_f$ ) ranges from 0.82 to 0.93, indicating that the passive film formed on the surface is relatively homogenous and compact. Moreover, at a fixed stress level, the passive film resistance of sample under primary passive state is the largest, followed by the sample under spontaneous passivation state and secondary passivation state. For example, for 90%σ<sub>s</sub>, the  $R_f$  of sample polarized at 0.2 V is  $3.13 \pm 0.02 \times 10^5 \Omega \cdot \text{cm}^2$ , and twice more than that of sample without polarization ( $1.45 \pm 0.04 \times 10^5 \Omega \cdot \text{cm}^2$ ) and polarized at 0.9 V ( $1.20 \pm 0.02 \times 10^5 \Omega \cdot \text{cm}^2$ ). It indicates that passivation state significantly changes the surface condition. Similarly, at a certain potential, the  $R_f$  gradually decreases with increasing stress, suggesting that stress also has a negative influence.

Fig. 8 presents parameters obtained from EIS data, which can reveal the passivation properties of 2205 DSS under different stress. Fig. 8(a) shows that film resistance  $R_f$  decreases with the increase of stress, suggesting that stress accelerates the film dissolution. Moreover, the value

of  $R_f$  fluctuates with the increase of anodic potential for samples with no stress and 30%σ<sub>s</sub>, which is corresponding to the well-passivated potential range in the potentiostatic polarization curves (Fig. 6c). However, when stress continues to increase,  $R_f$  decreases with increasing anodic potential, which is consistent with Fig. 6(c). This is because stress promotes the dissolution of passive film, concealing the thickness increase.

The effective capacitance  $C_{\text{eff}}$  can be calculated by the following equation [40]:

$$C_{\text{eff}} = Y_0^{\frac{1}{n}} R_s^{\frac{1-n}{n}} \quad (4)$$

where  $Y_0$  and  $n$  are the magnitude and dispersion coefficient of  $Q_f$ , respectively, and  $R_s$  is solution resistance. As shown in Fig. 8(b), the reciprocal of effective capacitance  $C_{\text{eff}}^{-1}$  changes linearly with the anodic potential, in which the slope is corresponding to the electric field strength  $E_0$  across the passive film according to Bojinov [41]:

$$\frac{dC_{\text{eff}}^{-1}}{dE} = \frac{1-\alpha}{\epsilon\epsilon_0 E_0} \quad (5)$$

where  $\alpha$  is the polarizability of the solution/film interface ( $\alpha=0.7$  [42]),  $\epsilon$  is the dielectric constant (15.6) and  $\epsilon_0$  is the vacuum permittivity ( $8.854 \times 10^{-14} \text{ F/cm}$ ). As presented in Fig. 8(d), the  $E_0$  values are in the range of 1.5–2.5 MV/cm, which is consistent with the description of the PDM. Moreover,  $E_0$  nearly increases linearly to 2.47 MV/cm as the stress increased to 90%σ<sub>s</sub>, which would promote the migration of point defects across the passive film. As mentioned above, the passive film can be described as a parallel-plate capacitor, and the film thickness ( $d$ ) can be expressed as [43]:

$$d = \frac{\epsilon\epsilon_0 A}{C_{\text{eff}}} \quad (6)$$

where  $A$  is the area of passive film. As Wallinder et al. stated, the effective area is about double of the geometric area for passive film, thus roughness factor of 2 is presumed [44]. As presented in Fig. 8(c), the film thickness is in the range of 1.75–3.75 nm, which agrees with previous works. In addition, the film thickness decreases with stress, which is attributed to higher dissolution rate of passive film. The film formation ratio ( $r$ ) can be derived from the linear relationship between  $d$  and  $E$  [26, 34]:

$$d = rE + B \quad (7)$$

where  $B$  is a constant depends on physicochemical conditions and the electrochemical reaction kinetics. The film formation ratio reduces with the growth of stress, indicating the facilitated film dissolution process (Fig. 8(d)).

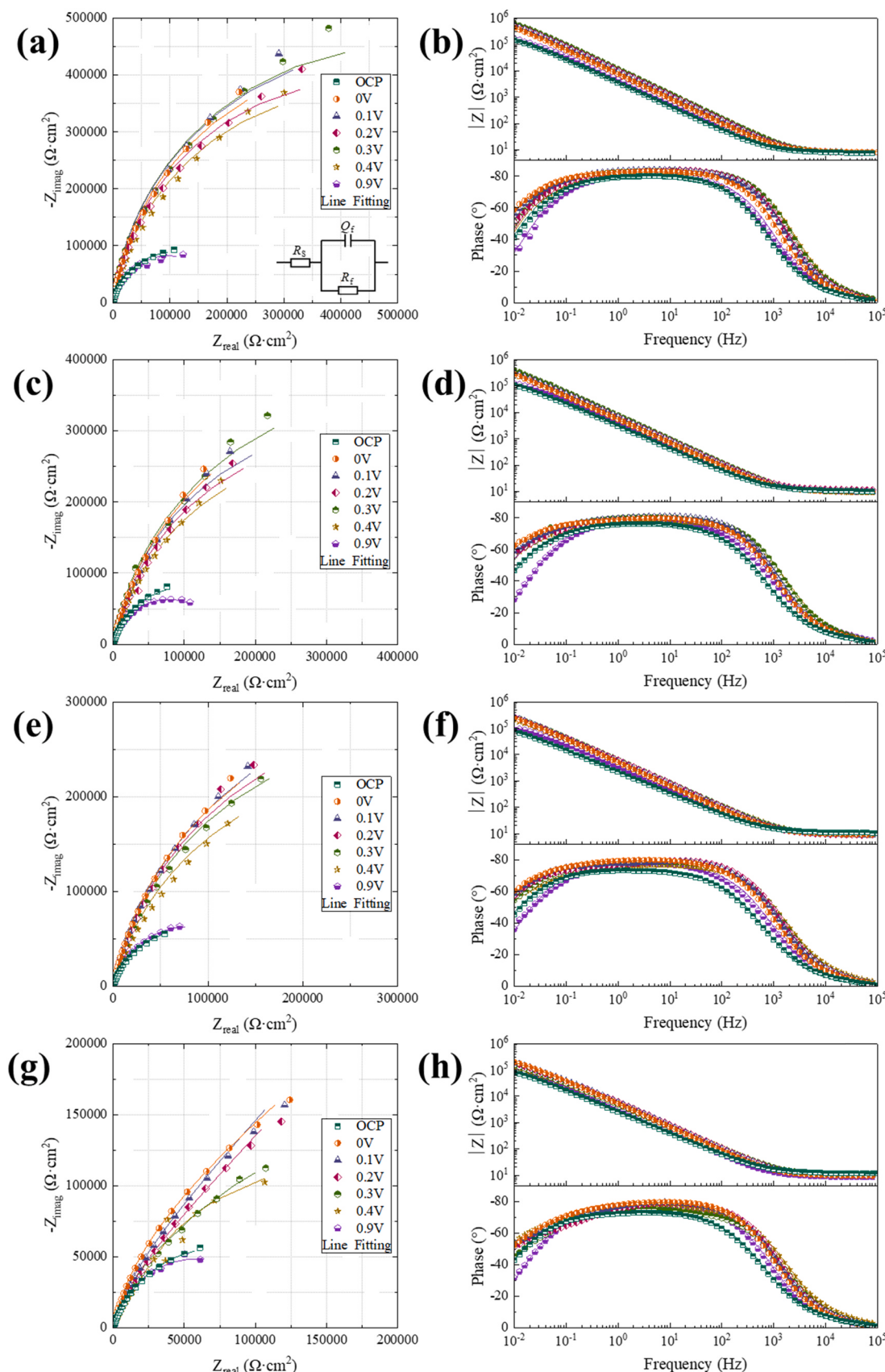


Fig. 7. Nyquist (a, c, e, g) and Bode plots (b, d, f, h) of 2205 DSS applied to  $0\%\sigma_s$  (a, b),  $30\%\sigma_s$  (c, d),  $60\%\sigma_s$  (e, f) and  $90\%\sigma_s$  (g, h) at different potentials.

**Table 1**

Typical fitted parameters for EIS data of 2205 DSS subject to different stress at different potentials.

Stress	Potential	$R_s$ V vs. Ag/ AgCl	$Q_f$		$R_f$ $\times 10^5 \Omega \cdot \text{cm}^2$
			$Y_0$ $\times 10^{-5} \Omega^{-1} \cdot \text{cm}^2 \cdot \text{s}^n$	$n$	
0% $\sigma_s$	OCP	$7.93 \pm 0.05$	$6.09 \pm 0.03$	$0.88 \pm 0.01$	$2.14 \pm 0.05$
	0.2	$8.05 \pm 0.06$	$1.85 \pm 0.01$	$0.93 \pm 0.01$	$8.34 \pm 0.20$
	0.9	$8.32 \pm 0.05$	$4.23 \pm 0.02$	$0.90 \pm 0.01$	$1.95 \pm 0.03$
30% $\sigma_s$	OCP	$9.49 \pm 0.07$	$7.05 \pm 0.04$	$0.85 \pm 0.01$	$2.04 \pm 0.06$
	0.2	$9.59 \pm 0.08$	$3.06 \pm 0.02$	$0.88 \pm 0.01$	$6.90 \pm 0.02$
	0.9	$9.09 \pm 0.07$	$4.43 \pm 0.03$	$0.87 \pm 0.01$	$1.65 \pm 0.03$
60% $\sigma_s$	OCP	$9.80 \pm 0.06$	$9.39 \pm 0.06$	$0.82 \pm 0.01$	$1.70 \pm 0.06$
	0.2	$8.84 \pm 0.06$	$3.40 \pm 0.02$	$0.88 \pm 0.01$	$6.62 \pm 0.25$
	0.9	$9.95 \pm 0.07$	$5.88 \pm 0.03$	$0.86 \pm 0.01$	$1.57 \pm 0.03$
90% $\sigma_s$	OCP	$9.78 \pm 0.08$	$8.74 \pm 0.05$	$0.82 \pm 0.01$	$1.45 \pm 0.04$
	0.2	$9.32 \pm 0.05$	$3.28 \pm 0.03$	$0.89 \pm 0.01$	$3.13 \pm 0.02$
	0.9	$8.58 \pm 0.06$	$6.22 \pm 0.04$	$0.87 \pm 0.01$	$1.20 \pm 0.02$

### 3.5. Mott-schottky analysis

In order to further investigate the semiconductor properties of the passive film, Mott-Schottky measurements are employed. According to Mott-Schottky theory, the space charge capacitance under the depletion condition can be calculated by the following equation [45]:

$$\frac{1}{C^2} = \pm \frac{2}{\epsilon \epsilon_0 e N} \left( E - E_{fb} - \frac{kT}{e} \right) \quad (8)$$

where  $C$  is the electrochemical capacitance of the passive film/electrolyte interface,  $e$  is the electronic charge ( $1.6 \times 10^{-19} \text{ C}$ ),  $N$  is the charge carrier density, the donor density  $N_D$  for n-type or the acceptor density  $N_A$  for p-type semiconductors,  $E_{fb}$  is the flat-band potential,  $k$  is the Boltzman constant ( $1.38 \times 10^{-23} \text{ J/K}$ ),  $T$  is the absolute temperature,  $\epsilon$ ,  $\epsilon_0$  and  $E$  have the same physical meaning as above.

Normally, the capacitance tends to increase with decreasing frequency, but it nearly maintains at a constant value in the range of 1 kHz and 10 Hz [46]. At higher frequencies, the capacitance grows because of OH adsorption at the oxide or the enhancement of parallel capacitance with the angular frequency of AC signal. At lower frequencies, the capacitance rises rapidly again because of low mobility of ionic species located in the space charge layer. In order to eliminate the capacitance dependence on the frequency from the influence of ionic species in the space charge layer, the maximum frequency within the region of nearly constant capacity should be chosen. Therefore, Mott-Schottky measurements are conducted as 1 kHz like many scholars [5,46].

The Mott-Schottky plots recorded for spontaneous passive film formed on 2205 DSS under different stress levels are presented in Fig. 9 (a), with the similar electronic character indicative of p-n heterojunction behavior. Depending on the potential, five linear regions can be observed in all these curves with a positive and negative slope characterized by different capacitance, agreeing with previous work [13,47]. A narrow potential plateau region, where the two oxides are in the so-called flat-band conditions, separating the first region ( $R_1$ ) and the second region ( $R_2$ ). Below  $-0.3 \text{ V}$  ( $R_1$ ), with negative slope, is characteristic of p-type semiconductors, suggesting that cation vacancies are the major defect in the passive film. The positive slope ( $R_2$ ) holds for an

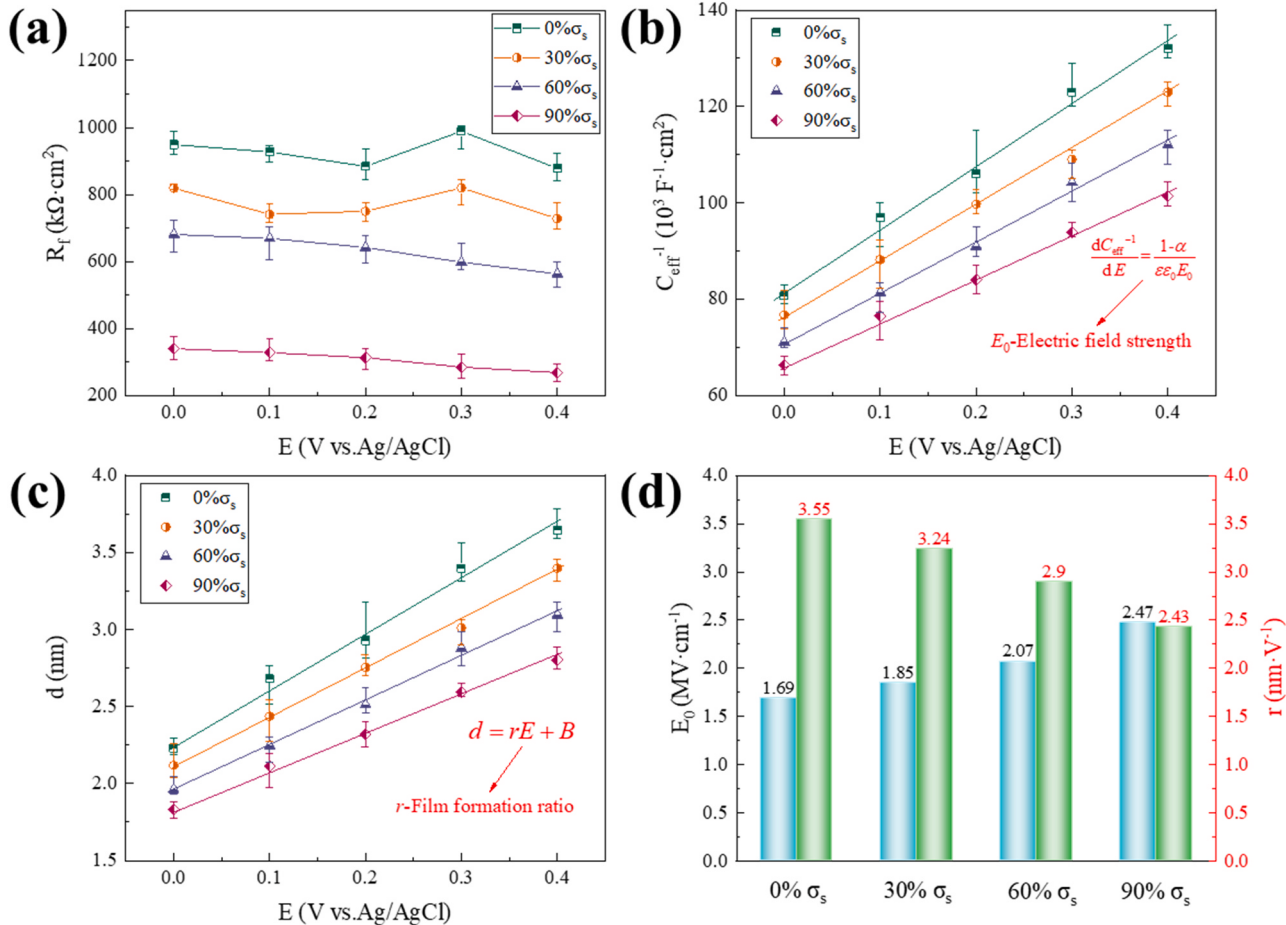


**Fig. 8.** Fitted film resistance  $R_f$  (a), reciprocal of effective capacitance  $C_{eff}^{-1}$  (b) and film thickness (c) at different anodic potential within well passivated region, and electric field strength and film ratio of passive film formed under different stress.

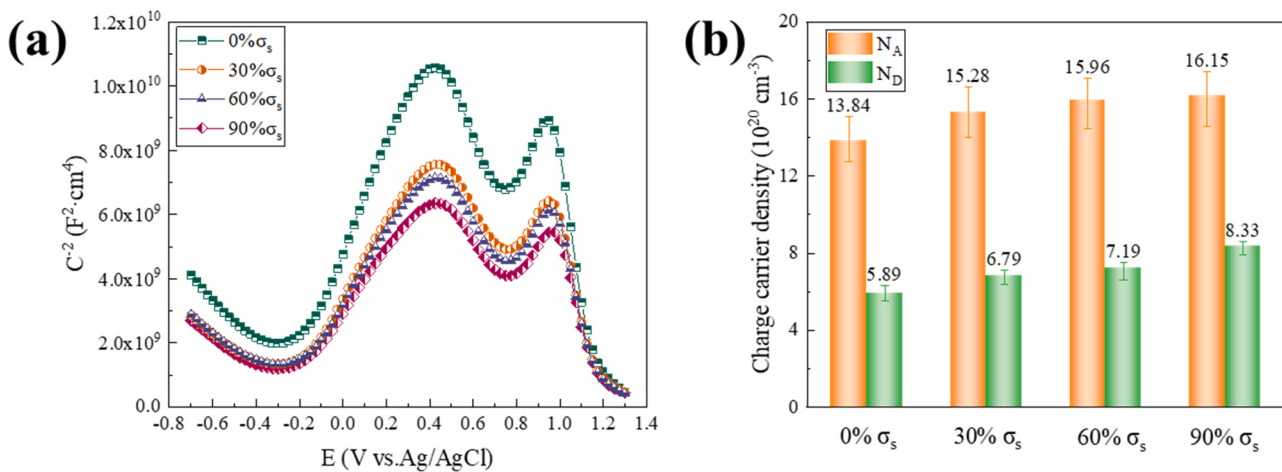


**Fig. 9.** Mott-Schottky curves of the self-passive film formed on 2205 DSS (a), and the calculated charge carrier density (b).

n-type semiconductor, suggesting that oxygen vacancies and/or cation interstitials are the predominant defect. The presence of two linear regions detected in the above Mott-Schottky curves are due to two different semiconducting layers, one inner layer is rich in p-type  $\text{Cr}_2\text{O}_3$ , one outer layer is rich in n-type  $\text{Fe}_2\text{O}_3$ , with a spinel structure [48,49]. Consequently, the negative slope ( $R_1$ ) is related to the presence of  $\text{Cr}_2\text{O}_3$ , while the positive slope ( $R_2$ ) is characteristic of  $\text{Fe}_2\text{O}_3$ . In the region  $R_3$  (0.45–0.75 V), the oxide film formed on the sample characterizes p-type semiconductor property with a calculated value, but no direct relationship between the semiconducting properties and charge carrier concentration can be established. The increase of capacitance is owing to the formation of an inversion layer due to an increasing hole concentration in the valence band [50]. For potentials comprising from 0.75 to 0.95 V ( $R_4$ ), a second n-type region presents, this is generally due to the presence of deep donor level in the band gap, which appears that the capacitance behaviour of the passive film is supported by a band structure model of the semiconductor electrode containing multiple donor levels in the bandgap. As the potential exceeds 0.95 V ( $R_5$ ), the slopes change to negative again, which can be attributed to the cation vacancies generated from the transpassive dissolution of  $\text{Fe}(\text{II})/\text{Fe}(\text{III})$  to  $\text{FeO}_3^{2-}$  following the oxidative dissolution of  $\text{Cr}(\text{III})$  to  $\text{Cr}(\text{VI})$  in  $R_3$  [25].

The values of the charge carrier density of spontaneous passive film formed on 2205 DSS is shown in Fig. 9(b). In the present study, all the calculated acceptor densities ( $N_A$ ) are from the  $R_1$  and donor densities ( $N_D$ ) are from the first donor level ( $R_2$ ). The  $N_D$  and  $N_A$  values are  $10^{20}$ – $10^{21} \text{ cm}^{-3}$  in the order of magnitudes, which shows similar results with literatures reported for stainless steels in different environment [5,25, 30]. Such high values mean that passive film formed on 2205 DSS is highly disordered. As presented in Fig. 9(b), the  $N_D$  increases from  $5.89 \times 10^{20}$  to  $8.33 \times 10^{20} \text{ cm}^{-3}$  as stress increases from 0% to 90% $\sigma_s$ . The  $N_A$  shows the similar tendency with  $N_D$ , the same results are also detected by Vignal et al. [17] and Feng et al. [13]. It is because the doping of the outer hydroxide depends on the stress level [17]. According to the description of point defects by Tanahashi and Inoue [51], the elastic tensile stress results in an increment in the formation of interstitials due to the change of volume. Because the major charge carriers in the space layer are oxygen vacancies and cation interstitials in this paper, it can be speculated that the elastic tensile stress accelerates the formation of cation interstitials. Generally, a higher  $N_D$  means that the stability of passive film is worse and the electrochemical reaction at the film/solution becomes more active. Therefore, this process promotes the dissolution of passive film. In addition, the value of  $N_D$  agrees with the film resistance of EIS results, as shown in Fig. 8(a).

Fig. 10(a)–(d) illustrates the typical Mott-Schottky curves of 2205 DSS measured at different film formation potentials under four different stress conditions. Passive film formed on 2205 DSS exhibits n-type

semiconductor behavior under all conditions, which is evidenced by the generally positive slope within the sweep potential range. It shows that the major charge carriers in the space charge layer are electrons and the impurities states are donor states. The plots almost overlap with each other when samples subjected to 90% $\sigma_s$ , which is attributed to simultaneous effect of potential and stress.

Fig. 10(e) presents the calculated donor densities of passive film formed under different conditions. Values of  $N_D$  are  $10^{20} \text{ cm}^{-3}$  in the order of magnitudes. Moreover,  $N_D$  is larger for samples with higher stress. It is also observed that the donor carrier density decreases with the increase of film formation potential when the stress is less than 90% $\sigma_s$ , because anodic polarization can eliminate some defects in the passive film and then the passive film becomes more compact [34]. However,  $N_D$  fluctuates with potential when the stress reaches at 90% $\sigma_s$ , indicating that such high elastic stress introduces remarkable difference to the surface. PDM implies that  $N_D$  is associated with the generation rate at metal/film interface and the annihilation rate at film/solution interface, and both two rates increase as the formation potential shifts to more noble [26]. Hence, the generation rate has a larger growth for 90% $\sigma_s$  sample compared to sample subjected to lower stress, and this is consistent with Fig. 6(c).

From previous literatures, the relationship between  $N_D$  and  $E$  can be described as [32,52]:

$$N_D = \omega_1 \exp(-bE) + \omega_2 \quad (9)$$

where  $\omega_1$ ,  $b$  and  $\omega_2$  are the parameters derived from fitting results, shown in Fig. 10(e). Diffusion coefficient ( $D_0$ ) of point defects is a key parameter to reflect the transport of points defects and the film properties, and because the  $E_0$  values are in the range of 1.5–2.5 MV/cm (Fig. 8d), the following equation is more proper [41]:

$$D_0 = \frac{zal_{ss}}{\omega_2 e \text{EXP}(zaE_0 F / RT)} \quad (10)$$

where  $a$  is the half-jump distance of the migrating point defect (0.4 nm [53]),  $z$  is the charge number of mobile point defect (2),  $F$  is the Faraday constant (96485 C/mol),  $R$  is the gas constant (8.314 J/K·mol) and other parameters are same as above. Thus,  $D_0$  are  $3.40 \times 10^{-18} \text{ cm}^2/\text{s}$  and  $3.88 \times 10^{-18} \text{ cm}^2/\text{s}$  for specimen without stress and with 30% $\sigma_s$ , respectively. Moreover, the values of  $D_0$  increase from  $4.14 \times 10^{-18} \text{ cm}^2/\text{s}$  to  $5.19 \times 10^{-18} \text{ cm}^2/\text{s}$  for 60% $\sigma_s$  specimens as the potential increased from 0 V to 0.4 V. The increase of  $D_0$  may promote pit initial rate and passive film localized breakdown [54].

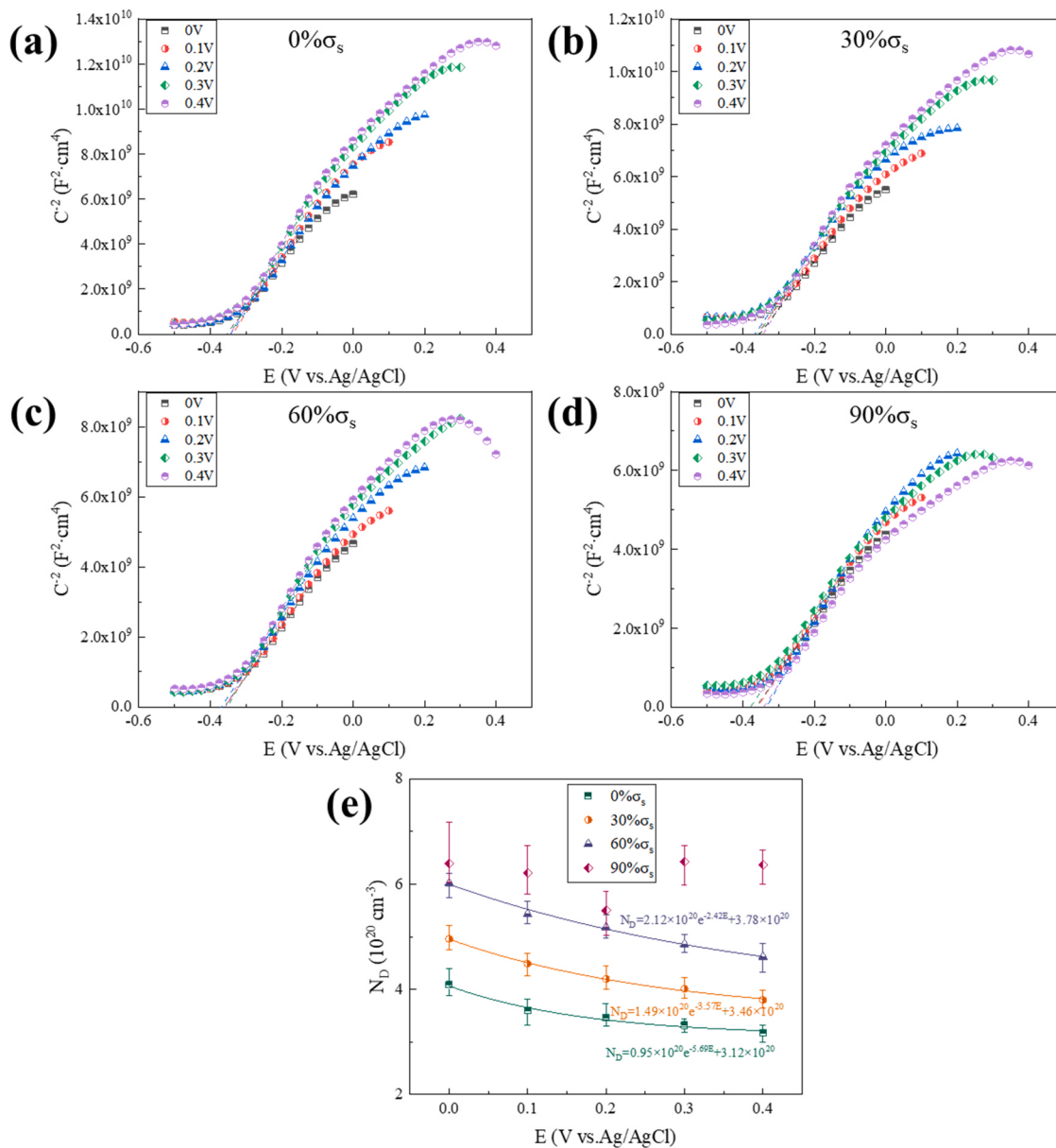


**Fig. 10.** Mott-Schottky curves of the passive film formed at different potential on 2205 DSS under  $0\%\sigma_s$  (a),  $30\%\sigma_s$  (b),  $60\%\sigma_s$  (c), and  $90\%\sigma_s$  (d), as well as the calculated donor carrier density(e).

### 3.6. XPS analysis

The stability, protective character and semiconducting properties of passive film are strongly related to the composition, and thus XPS is employed. Fig. 11 displays the high dissolution XPS of Fe 2p<sub>3/2</sub>, Cr 2p<sub>3/2</sub> and O 1s of the passive film formed on 2205 DSS and corresponding ratios of  $Fe^{2+}/Fe^{3+}$ ,  $Cr_{ox}/Cr_{hy}$ ,  $O^{2-}/OH^-$  and  $Fe_{ox+hy}/Cr_{ox+hy}$ . The binding energy of each constituent used for fitting is presented in Table 2. It should be noted that  $Fe_3O_4$  is treated as  $FeO \cdot Fe_2O_3$  in the calculation of  $Fe^{2+}/Fe^{3+}$  percentage. It can be seen that the composition of outmost layer of passive film is complex, which is mainly composed of oxides and hydroxides of iron and chromium.

As shown in Fig. 11(d), the  $Fe^{2+}/Fe^{3+}$  ratio increases continuously with increasing tensile stress, indicating that the stability of passive film is degraded. As the  $Fe^{2+}$  specie in passive film increases, due to the doping state of  $Fe^{2+}$ , more oxygen vacancies are formed in passive film as the electric charges balance [55]. Meanwhile, the Fe(III)-contain constituents are the main iron oxidized compositions in the passive

film because  $Fe^{2+}/Fe^{3+}$  ratios are all small than 1 in spite of different stress. In terms of Cr, three contributions (metallic Cr,  $Cr_2O_3$  and  $Cr(OH)_3$ ) are detected for no stress and  $30\%\sigma_s$  samples. Whereas, the peak of  $CrO_3$  is surprisingly observed for specimens subjected to  $60\%\sigma_s$  and  $90\%\sigma_s$ , which should not be present in the passive film based on E-pH diagrams. According to the work of Olsson [56],  $CrO_3$  can coexist with  $Cr_2O_3$  in passive film because of their similar standard free enthalpies. Even though there is no sufficient and direct evidence to demonstrate the connection between the presence of  $CrO_3$  in the passive film and passivation behavior of stainless steel, Luo et al. [47] observed the appearance of  $CrO_3$  in samples with cold formation occurred simultaneously with the relatively lower corrosion resistance. This indicates that the corrosion resistance of samples with  $60\%\sigma_s$  and  $90\%\sigma_s$  becomes worse, agreeing with the above results. Furthermore, the  $Cr_{ox}/Cr_{hy}$  ratio gradually increases to close to 1 when specimen is subjected to higher stress, suggesting that the percentage of  $Cr(OH)_3$  decreases but  $Cr(OH)_3$  is still the dominant species. Moreover, the ratio of  $O^{2-}/OH^-$  increases with stress in the spectra of O1s, implying the increase of oxides and/or

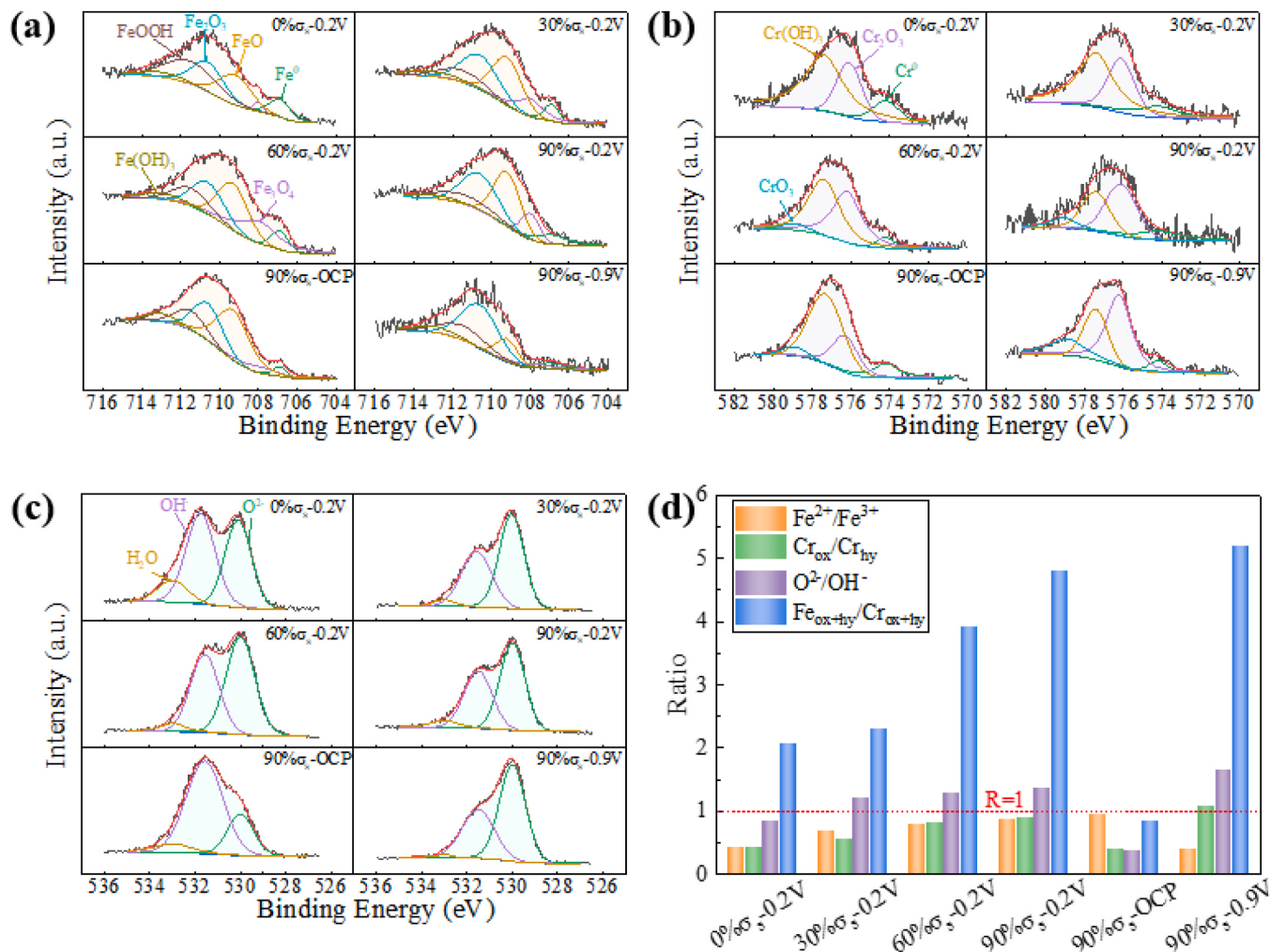


**Fig. 11.** The high resolution XPS of Fe 2p<sub>3/2</sub> (a), Cr 2p<sub>3/2</sub> (b) and O 1 s (c) of the passive film formed at 0.2 V on 2205 DSS under different stress and potential, and corresponding ratios of Fe<sup>2+</sup>/Fe<sup>3+</sup>, Cr<sub>ox</sub>/Cr<sub>hy</sub>, O<sup>2-</sup>/OH<sup>-</sup> and Fe<sub>ox+hy</sub>/Cr<sub>ox+hy</sub> (d).

**Table 2**  
Binding energy of XPS peaks applied for fitting.

Fe2p <sub>3/2</sub>	Constituents	Fe <sup>0</sup>	Fe <sub>3</sub> O <sub>4</sub>	FeO	Fe <sub>2</sub> O <sub>3</sub>	FeOOH	Fe(OH) <sub>3</sub>
Cr2p <sub>3/2</sub>	Constituents	Cr <sup>0</sup>	Cr <sub>2</sub> O <sub>3</sub>	Cr(OH) <sub>3</sub>	CrO <sub>3</sub>		
O1s	Constituents	O <sup>2-</sup>	OH <sup>-</sup>	H <sub>2</sub> O			
	Binding Energy (eV)	706.9 ± 0.1	708.0 ± 0.1	709.2 ± 0.1	710.6 ± 0.1	711.5 ± 0.1	713.0 ± 0.2
		574.2 ± 0.1	576.1 ± 0.1	577.4 ± 0.1	578.9 ± 0.1		
		530.0 ± 0.1	531.7 ± 0.2	533.0 ± 0.2			

decrease of hydroxides. As suggested by Luo et al. [47], the chemisorbed water (H<sub>2</sub>O-M-H<sub>2</sub>O) plays an important role in the stability of passive film, it could not only participate the self-repairing action of the passive film but also capture the dissolving metal ions and form protective layer. It is found that stress reduces the content of chemisorbed water (533 eV) in passive film, showing injurious effects on the corrosion resistance of 2205 DSS. The increase of Fe<sub>ox+hy</sub>/Cr<sub>ox+hy</sub> with increasing stress suggests that the percentage of chromium decreases in outer layer, leading to worse protection. And the ratio of Fe<sub>ox+hy</sub>/Cr<sub>ox+hy</sub> are all above 1, indicating that oxidized Fe dominates the composition of passive film.

Three different passivation states, i.e., spontaneous passivation (OCP), primary passivation (0.2 V) and secondary passivation (0.9 V) are investigated because the applied potential also has significant effects on passive film. The Fe<sup>2+</sup>/Fe<sup>3+</sup> ratio reduce monotonously when noble potential applied, which is attributed to the transformation from Fe(II) to Fe(III) compounds, as presented in Fig. 11(d). The variation of Cr is

dominated by the increase of oxides and the decrease of hydroxides, resulting in the increase of Cr<sub>ox</sub>/Cr<sub>hy</sub> ratio with potential. At the same time, the ratio of O<sup>2-</sup>/OH<sup>-</sup> and Fe<sub>ox+hy</sub>/Cr<sub>ox+hy</sub> increase with increasing imposed potential. These similar results are also found in previous literatures [5,25,57,58], this is because the increasing film formation potential introduces a small degree of hydration and thus decreases the carrier densities.

In order to further analyze the depth distribution of species within the passive film, the detailed Fe, Cr and O spectra are investigated, as exhibited in Fig. 12. As the sputtering time prolongs, the signal of Fe<sup>0</sup> strengthens but that of Fe oxides weakens for both specimens without stress and with 90%σ<sub>s</sub>. The same tendency can be observed in peaks of Cr<sup>0</sup> and Cr oxides. In addition, the O element can be still detected even after sputtering for 110 s due to oxygen pollution, which indicates that the adsorption rate of oxygen as impurity in argon is closely equivalent to the removal rate of oxide film on the sample as the sputtering etching

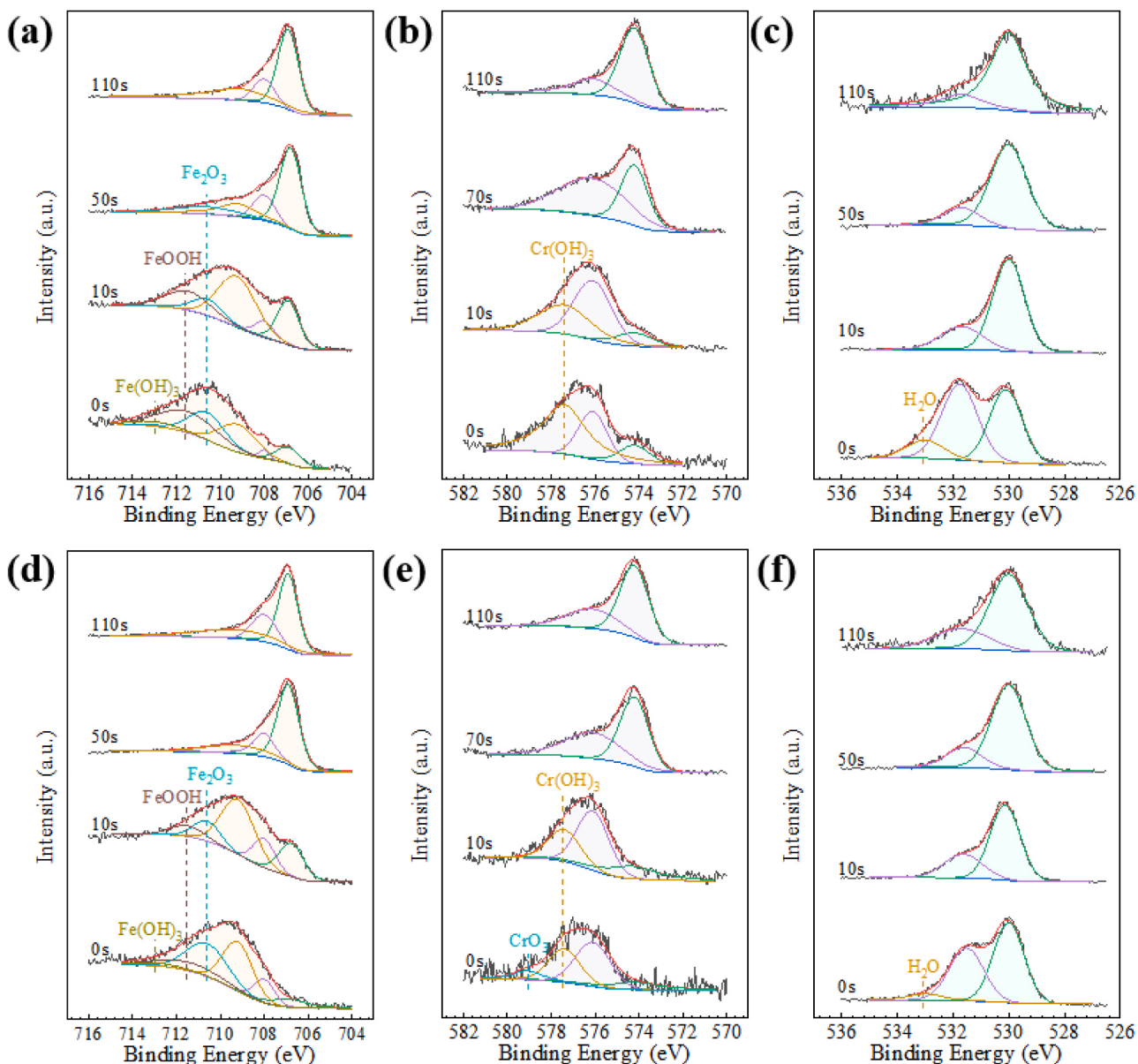


**Fig. 12.** The high resolution XPS of Fe 2p<sub>3/2</sub> (a, d), Cr 2p<sub>3/2</sub> (b, e) and O 1 s (c, f) with sputtering time of the passive film formed at 0.2 V on 2205 DSS without stress (a, b, c) and with 90% $\sigma_s$  (d, e, f).

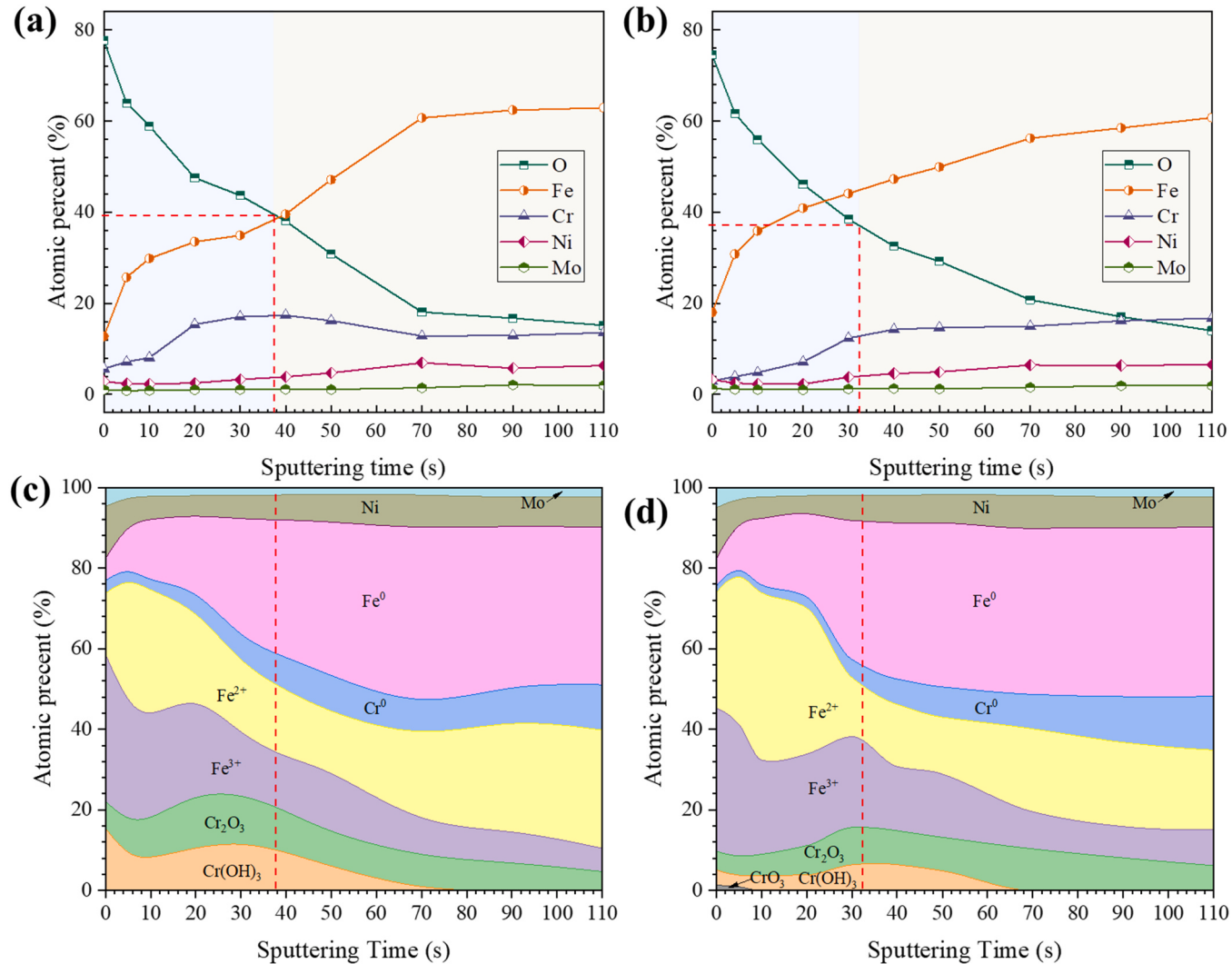
approaches the film substrate interface [59]. Because of this, it is difficult to define a sharp film/metal interface, where the oxygen concentration should change from that of oxide stoichiometry to zero in theoretically. With the increase of sputtering time, peaks of Fe(OH)<sub>3</sub> and FeOOH cannot be observed gradually for both two samples. After sputtering for 50 s, the peak of Fe<sub>2</sub>O<sub>3</sub> still exists for the sample without stress, while it disappears for the sample with 90% $\sigma_s$ . It indicates that Fe (III) compounds mainly exist in the outer layer of passive film and stress can decrease its thickness. Cr spectra show similar variation with Fe spectra, Cr<sub>2</sub>O<sub>3</sub> only exists in the outmost layer and it cannot be detected even after 10 s for 90% $\sigma_s$  sample, but more time is needed for Cr(OH)<sub>3</sub> to disappear for both two samples (Fig. 12(b) and (e), Fig. 13(c) and (d)).

Fig. 13 shows the atomic percent depth profiles of elements and distribution of different components. It should be noted that the half of O element in the passive film is considered as its corresponding thickness. The thickness marked in the pictures for samples without stress and with 90% $\sigma_s$  are about 3.78 nm and 3.21 nm, i.e., 37.8 s and 32.1 s for sputtering time (Fig. 13(a) and (b)), respectively. Moreover, the outer layer of the passive film formed on the sample with 90% $\sigma_s$  stress has higher Fe

content and lower Cr and O content than that formed on the sample without stress, demonstrating that stress reduces the thickness of passive film and accelerates the dissolution of Cr. After normalization treatment, the percentage of different compounds can be calculated and the results are presented in Fig. 13(c) and (d). According to the PDM, the passive film can be divided into an outer layer and an inner layer, but these two layers are difficult to be clearly distinguished through XPS results since the contamination of oxygen conceals boundary characters. However, the distribution of Fe and Cr compounds shows that Fe is enriched in the outer layer and Cr in the inner layer. To be more precise, the outer layer is dominated by Fe(III) compounds and the inner layer mainly consists of Cr<sub>2</sub>O<sub>3</sub> and Fe(II) compounds [25]. Additionally, the percentages of Fe and Cr in the passive film are more than 80% and increase gradually to the value for the matrix.

#### 4. Discussion

Based on the above results, the effect of elastic stress on the passivation characteristics is summarized in Table 3.



**Fig. 13.** XPS depth profiles of elements (a, b) and distribution of different components (c, d) within the passive film formed at 0.2 V on 2205 DSS without stress (a, c) and with 90%σ<sub>s</sub> (b, d).

#### 4.1. Effect of elastic stress on the passive film formation kinetics

Fig. 14 shows the schematic diagram of the effect of elastic stress on the passive film formation kinetics. It is accepted that the passive film formation process is in a dynamic equilibrium state, and determined by two sides, i.e., growth at the metal/film interface and dissolution at the film/solution interface. The elastic stress can lead to localized lattice distortion and higher activation energy [13,15], and metal dissolution preferentially occurs, then accelerating the nucleation of passive film, as demonstrated by the increase of LAGB and KAM and the decrease of Σ3 twin boundaries in Figs. 2 and 3. This effect will lead to higher reaction rate for the specimen with stress, and thus higher growth rate of passive film. Because of higher growth rate, the diffusion time of atoms, ions and electrons to the "right" position is limited, and more defects will be generated in the passive film [33]. Meanwhile, the elastic tensile stress can promote the generation of cation interstitials [51]. As a result, the donor density will increase when a specimen is subjected stress, as shown in Figs. 9 and 10. As reported in literatures, the film dissolution rate  $i_d$  is a function of the potential drop at film/solution interface  $\varphi_{f/s}$ , which is the decisive factor controlling the dissolution rate of passive film, and can be calculated by the following expression [16,60–62]:

$$i_d = i_d^0 \exp\left(\frac{amF\varphi_{f/s}}{RT}\right) \quad (11)$$

$$\varphi_{f/s} = \Delta E - \varphi_{m/f} - \varphi_f \quad (12)$$

where  $i_d^0$  is the exchange current density,  $\alpha$  is the symmetry coefficient,  $m$  is the number of electrons,  $\Delta E$  is the applied potential,  $\varphi_{m/f}$  is the potential drop at the metal/film interface and  $\varphi_f$  is the potential drop within film ( $E_0 \times d$ ). EIS and XPS results show that the film thickness  $d$  is significantly decreased by stress, while  $E_0$  is increased modestly (Figs. 8 and 13). As a result, the  $\varphi_{f/s}$  increases with stress, accelerating the film dissolution process. Even though the growth and dissolution rates increase with stress, the increment in the dissolution rate of passive film is more remarkable, and thus decreasing formation rate of passive film, OCP value  $E$  (Fig. 4) and film formation ratio  $r$  (Fig. 8). Meanwhile, passive current density (Fig. 5) and quasi-steady-state current density  $I_{ss}$  (Fig. 6) increase. Nevertheless, according to the PDM, the  $I_{ss}$  of an n-type semi-conductive passive film is related to the density ( $N_D$ ) and the diffusion coefficient ( $D_0$ ) of point defects through the passive film [63]:

$$I_{ss} = 4FKD_0N_D \quad (13)$$

Hence, the increase of  $I_{ss}$  is also demonstrated by the increment in  $N_D$  and  $D_0$ .

**Table 3**

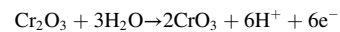
Summary of elastic stress on the passivation characteristics of 2205 DSS.

	Trends when stress increases	Indication
Open circuit potential, $E$	-	
passive current density	+	
Steady-state passive current density, $I_{ss}$	+	Higher film growth and dissolution rate
Potential drop at film/ solution interface, $\varphi_{f/s}$	+	
Electric field strength across the passive film, $E_0$	+	
Film growth ration, $r$	-	
Passive film resistance, $R_f$	-	Lower film formation rate and film protectiveness
Donor density, $N_D$	+	Higher surface energy density, reaction activity and film dissolution rate
Diffusion coefficient of defects, $D_0$	+	
Passive film thickness, $d$	-	
$Fe^{2+}/Fe^{3+}$	+	
$Cr_{ox}/Cr_{hy}$	+	
$O^{2-}/OH^-$	+	
$Fe_{ox+hy}/Cr_{ox+hy}$	+	

+ represents increase; - represents decrease

#### 4.2. Effect of elastic stress on the passive film composition

As mentioned above, the surface activity is improved by the elastic stress, and thus passive film composition is changed. Stress promotes the dissolution of Fe(III), contributing to the increment in  $Fe^{2+}/Fe^{3+}$  ratio (Fig. 11). Then the increase of Fe(II) percentage leads to the growth in donor density due to Fe(II) is the main cation interstitial (Fig. 10). Moreover, when sample is subjected to 60% or 90% $\sigma_s$ , CrO<sub>3</sub> generates [25,64]:



and/or:



And CrO<sub>3</sub> is related to soluble chromium ions Cr<sub>2</sub>O<sub>4</sub><sup>2-</sup>, which contribute to the dissolution process of the passive film. Although the passive film is not breakdown in this work, the slight transpassive dissolution may cause the slight increment in the donor density. Besides, the dissolution of Cr(III) is more notable than that of Fe(III), leading to the increase of  $Fe_{ox+hy}/Cr_{ox+hy}$  within the surface layer. The tensile elastic stress also has a dehydration effect, which results in an increase of O<sup>2-</sup>/OH<sup>-</sup> ratio. As a result, the protectiveness of the passive film decreases, as shown in Fig. 8. The passive film thickness is also reduced by the elastic stress as demonstrated by EIS and XPS results. The calculated film thickness obtained from the effective capacitance  $C_{eff}$  of EIS results for 0% and 90% $\sigma_s$  samples formed at 0.2 V are approximately 2.93 nm and 2.32 nm (Fig. 8), respectively. This agrees with XPS depth profiles, in which the equivalent thicknesses simply estimated using the half-height of O element are about 3.78 nm and 3.21 nm (Fig. 13), respectively, which proves thinning of the passive film after subjecting stress, although this method is not very precise due to oxygen pollution and destruction by sputtering.

#### 4.3. Character of passive film under different passivation states

Passive film formed under OCP is considered as spontaneous passivation state, the film is relatively thin and less protective due to low driving force to three-dimensional growth of oxide particles and their coalescence [5]. According to previous literatures [25], the rates of the nucleation and growth process of passive films are accelerated by overpotential. In other words, the number and size of oxide particles increase with increasing formation potential. As the anodic potential 0.2 V is applied, the oxidation of Fe(II) to Fe(III) is promoted at the interface between the inner and outer layers, as indicated by the

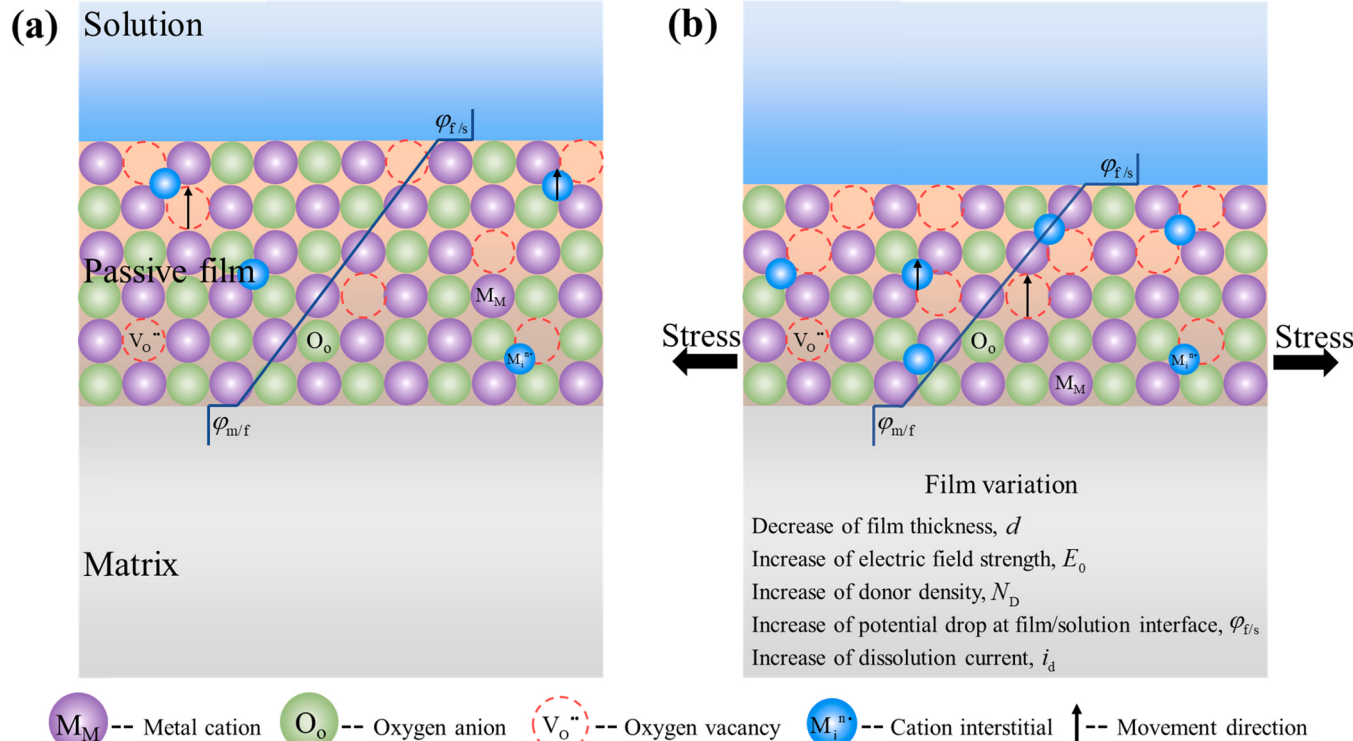


Fig. 14. Schematic diagram of the effect of elastic stress on the passive film formation kinetics for without stress (a) and with stress (b).

decrease of  $\text{Fe}^{2+}/\text{Fe}^{3+}$  in Fig. 11(d). During the film growth, the inner layer also becomes thicker, resulting in the increase in the thickness and compactness of passive film (Fig. 8). Meanwhile, potential also has a hydration effect, leading to the dominant composition transforms from hydroxides to oxides, as indicated by Fig. 11(d). As the film formation potential shifted to 0.9 V, the energy bands bend obviously and the Fermi-level is lower than the valence band edge at the outmost surface layer of the passive film [65], resulting in the transpassive dissolution of chromium. The dissolution of Cr(III) to Cr(VI) contributes to the increase of  $\text{Cr}_{\text{ox}}/\text{Cr}_{\text{hy}}$  and  $\text{Fe}_{\text{ox+hy}}/\text{Cr}_{\text{ox+hy}}$  ratios (Fig. 11d). Meanwhile, the Fe (III) compounds become the main composition due to its stability at high potential (Fig. 11d), this leads to a decrement of passivity and protectiveiveness of the passive film (Fig. 8).

## 5. Conclusion

The effect of tensile elastic stress on the electrochemical passivation behavior and surface chemistry of 2205 DSS has been investigated in this work. The main conclusions are as follows:

- (1) Even though elastic stress promotes the growth rate of passive film by modifying the surface state, it significantly accelerates the dissolution process by the increase in potential drop at the film/solution interface ( $\varphi_{\text{f/s}}$ ), donor density ( $N_D$ ) and diffusion coefficient of defects ( $D_0$ ), and thus leading to higher passive current density and quasi-steady-state current density and lower open circuit potential and film resistance.
- (2) High elastic stress ( $\geq 60\% \sigma_s$ ) leads to the generation of soluble  $\text{CrO}_3$ , the increase of oxidized Cr and Fe(II) content and the decrease of film thickness, which results in the increment of quasi-steady-state current density with the increase of anodic film formation potential.
- (3) A relatively thin and less protective passive film forms under spontaneous passivation state, while a denser film with lower  $\text{Fe}^{2+}/\text{Fe}^{3+}$  ratio is created in primary passive region due to higher rates of the nucleation and growth process of passive film. In the secondary passive region,  $\text{Cr}_{\text{ox}}/\text{Cr}_{\text{hy}}$  and  $\text{Fe}_{\text{ox+hy}}/\text{Cr}_{\text{ox+hy}}$  ratios increase remarkably because chromium is oxidized and dissolved at the layer surface, resulting in the decrease of film resistance, even lower than that under spontaneous passivation state.

## CRediT authorship contribution statement

**Longjun Chen:** Conceptualization, Methodology, Data curation, Writing – original draft, Writing – review & editing. **Wei Liu:** Supervision, Writing – review & editing. **Baojun Dong:** Formal analysis. **Yonggang Zhao:** Software. **Tianyi Zhang:** Validation. **Yueming Fan:** Investigation. **Weijian Yang:** Visualization.

## Declaration of Competing Interest

The authors declare that they have no known competing financial interests or personal relationships that could have appeared to influence the work reported in this paper.

## Data Availability Statement

The raw/processed data required to reproduce these findings cannot be shared at this time as the data also forms part of an ongoing study.

## Acknowledgments

The authors are grateful to the National Natural Science Foundation of China (51571027) and the funding support from the National Key R&D Program of China (2016YFE0203600).

## Statement of originality

I would like to declare on behalf of my co-authors that the work described was original research that has not been published previously, and not under consideration for publication elsewhere, in whole or in part. Moreover, the work is not involving plagiarism with copyright infringement issues.

## References

- [1] J. Yao, D.D. Macdonald, C. Dong, Passive film on 2205 duplex stainless steel studied by photo-electrochemistry and ARXPS methods, Corros. Sci. 146 (2019) 221–232.
- [2] J. Pilhagen, R. Sandström, Influence of nickel on the toughness of lean duplex stainless steel welds, Mat. Sci. Eng. A-Struct. 602 (2014) 49–57.
- [3] G. Tranchida, M. Clesi, F.D. Franco, F.D. Quarto, M. Santamaria, Electronic properties and corrosion resistance of passive films on austenitic and duplex stainless steels, Electrochim. Acta 273 (2018) 412–423.
- [4] L. Guo, S. Qin, B. Yang, D. Liang, L. Qiao, Effect of hydrogen on semiconductive properties of passive film on ferrite and austenite phases in a duplex stainless steel, Sci. Rep. -UK 7 (2017) 3317.
- [5] Z. Cui, S. Chen, Y. Dou, S. Han, L. Wang, C. Man, X. Wang, S. Chen, Y.F. Cheng, X. Li, Passivation behavior and surface chemistry of 2507 super duplex stainless steel in artificial seawater: Influence of dissolved oxygen and pH, Corros. Sci. 150 (2019) 218–234.
- [6] H. Luo, H. Su, C. Dong, K. Xiao, X. Li, Influence of pH on the passivation behaviour of 904L stainless steel bipolar plates for proton exchange membrane fuel cells, J. Alloy. Compd. 686 (2016) 216–226.
- [7] M. Kumagai, S.T. Myung, Y. Katada, H. Yashiro, Stability of type 310S stainless steel bipolar plates tested at various current densities in proton exchange membrane fuel cells, Electrochim. Acta 211 (2016) 754–760.
- [8] L. Wang, Y. Dou, S. Han, J. Wu, Z. Cui, Influence of sulfide on the passivation behavior and surface chemistry of 2507 super duplex stainless steel in acidified artificial seawater, Appl. Surf. Sci. 504 (2019), 144340.
- [9] U. Martin, J. Ress, J. Bosch, D.M. Bastidas, Stress corrosion cracking mechanism of AISI 316LN stainless steel rebars in chloride contaminated concrete pore solution using the slow strain rate technique, Electrochim. Acta 335 (2020), 135565.
- [10] C. Örnek, D.L. Engelberg, Towards understanding the effect of deformation mode on stress corrosion cracking susceptibility of grade 2205 duplex stainless steel, Mat. Sci. Eng. A-Struct. 666 (2016) 269–279.
- [11] C. Örnek, S.A.M. Idris, P. Recagni, D.L. Engelberg, Atmospheric-induced stress corrosion cracking of grade 2205 duplex stainless steel-effects of 475°C embrittlement and process orientation, Metals 6 (2016) 167.
- [12] Y. Hou, J. Zhao, C. Cheng, L. Zhang, J. Li, B. Liu, T. Cao, The metastable pitting corrosion of 2205 duplex stainless steel under bending deformation, J. Alloy. Compd. 830 (2020), 154422.
- [13] X. Feng, X. Lu, Y. Zuo, D. Chen, The passive behaviour of 304 stainless steels in saturated calcium hydroxide solution under different deformation, Corros. Sci. 82 (2014) 347–355.
- [14] X. Feng, X. Zhang, Y. Xu, R. Shi, X. Lu, L. Zhang, J. Zhang, D. Chen, Corrosion behavior of deformed low-nickel stainless steel in groundwater solution, Eng. Fail. Anal. 98 (2019) 49–57.
- [15] R.K. Zhu, J.L. Luo, Investigation of stress-enhanced surface reactivity on Alloy 800 using scanning electrochemical microscopy, Electrochim. Commun. 12 (2010) 1752–1755.
- [16] X. Wang, H. Luo, J. Luo, Effects of hydrogen and stress on the electrochemical and passivation behaviour of 304 stainless steel in simulated PEMFC environment, Electrochim. Acta 293 (2018) 60–77.
- [17] V. Vignal, R. Oltra, M. Verneau, L. Coudreuse, Influence of an elastic stress on the conductivity of passive films, Mat. Sci. Eng. A-Struct. 303 (2001) 173–178.
- [18] D. Sidane, O. Devos, M. Puiggali, M. Touzet, B. Tribollet, V. Vivier, Electrochemical characterization of a mechanically stressed passive layer, Electrochim. Commun. 13 (2011) 1361–1364.
- [19] ASTM, G39–99, Standard practice for preparation and use of bent-beam stress-corrosion test specimens, 2021.
- [20] C. Fukuoka, K. Morishima, H. Yoshizawa, K. Mino, Misorientation development in grains of tensile strained and crept 2.25%Cr-1% Mo steel, Scr. Mater. 46 (2002) 61–66.
- [21] D. Song, A. Ma, W. Sun, J. Jiang, J. Jiang, D. Yang, G. Guo, Improved corrosion resistance in simulated concrete pore solution of surface nanocrystallized rebar fabricated by wire-brushing, Corros. Sci. 82 (2014) 437–441.
- [22] J.M.A.E. Kader, A.M.S.E. Din, Film thickening on nickel in aqueous solution in relation to anion type and concentration, Brit. Corros. J. 4 (1979) 40–45.
- [23] S.M.A.E. Haleem, E.E.A.E. Aal, S.A.E. Wanees, A. Diab, Environmental factors affecting the corrosion behaviour of reinforcing steel: I. The early stage of passive film formation in  $\text{Ca}(\text{OH})_2$  solutions, Corros. Sci. 52 (2010) 3875–3882.
- [24] L. Chen, J. Hu, X. Zhong, Q. Zhang, Y. Zheng, Z. Zhang, D. Zeng, Corrosion behaviors of Q345R steel at the initial stage in an oxygen-containing aqueous environment: experiment and modeling, Materials 11 (2018) 1462.
- [25] C. Man, C. Dong, Z. Cui, K. Xiao, Q. Yu, X. Li, A comparative study of primary and secondary passive films formed on AM355 stainless steel in 0.1 M NaOH, Appl. Surf. Sci. 427 (2018) 763–773.

- [26] D.D. Macdonald, On the existence of our metals-based civilization: I. phase-space analysis, *J. Electrochem. Soc.* 157 (2006) B213–B224.
- [27] B. Heine, R. Kirchheim, Dissolution rates of iron and chromium and Fe-Cr alloys in the passive state, *Corros. Sci.* 31 (1990) 533–538.
- [28] C. Escrivà-Cerdán, E. Blasco-Tamarit, D.M. García-García, J. García-Antón, R. Akid, J. Walton, Effect of temperature on passive film formation of UNS N08031 Cr-Ni alloy in phosphoric acid contaminated with different aggressive anions, *Electrochim. Acta* 111 (2013) 552–561.
- [29] Y. Qiao, Y. Zheng, W. Ke, P. Okafor, Electrochemical behaviour of high nitrogen bearing stainless steel in acidic chloride solution: effects of oxygen, acid concentration and surface roughness, *Electrochim. Acta* 54 (2009) 2298–2304.
- [30] H. Luo, H. Su, B. Li, G. Ying, Electrochemical and passive behaviour of tin alloyed ferritic stainless steel in concrete environment, *Appl. Surf. Sci.* 439 (2018) 232–239.
- [31] D.A. Jones, N.D. Greene, Electrochemical measurement of low corrosion rates, *Corrosion* 22 (1966) 198–205.
- [32] G.T. Burstein, B.T. Daymond, The remarkable passivity of austenitic stainless steel in sulphuric acid solution and the effect of repetitive temperature cycling, *Corros. Sci.* 51 (2009) 2249–2252.
- [33] A. Fattah-Alhosseini, M.A. Golozar, A. Saatchi, K. Raeissi, Effect of solution concentration on semiconducting properties of passive films formed on austenitic stainless steels, *Corros. Sci.* 52 (2010) 205–209.
- [34] R.M. Fernández-Domene, E. Blasco-Tamarit, D.M. García-García, J. García-Antón, Passive and transpassive behaviour of alloy 31 in a heavy brine LiBr solution, *Electrochim. Acta* 95 (2013) 1–11.
- [35] D. Li, J. Wang, D. Chen, Influence of potentiostatic aging, temperature and pH on the diffusivity of a point defect in the passive film on Nb in an HCl solution, *Electrochim. Acta* 60 (2012) 134–146.
- [36] D. Kong, W. Lu, Y. Feng, Z. Yu, J. Wu, W. Fan, H. Liu, Studying on the point-defect-conductive property of the semiconducting anodic oxide films on titanium, *J. Electrochem. Soc.* 156 (2009) C39–C44.
- [37] F. Mohammadi, T. Nickchi, M.M. Attar, A. Alfantazi, EIS study of potentiostatically formed passive film on 304 stainless steel, *Electrochim. Acta* 56 (2011) 8727–8733.
- [38] I. Nicic, D.D. Macdonald, The passivity of type 316L stainless steel in borate buffer solution, *J. Nucl. Mater.* 379 (2008) 54–58.
- [39] N. Priyantha, P. Jayaweera, D.D. Macdonald, A. Sun, An electrochemical impedance study of alloy 22 in NaCl brine at elevated temperature. I. Corrosion behavior, *J. Electroanal. Chem.* 572 (2004) 409–419.
- [40] G.J. Brug, A.L.G. van den Eeden, M. Sluyters-Rehbach, J.H. Sluyters, The analysis of electrode impedances complicated by the presence of a constant phase element, *J. Electroanal. Chem.* 176 (1984) 275–295.
- [41] M. Bojinov, The ability of a surface charge approach to describe barrier film growth on tungsten in acidic solutions, *Electrochim. Acta* 42 (1997) 3489–3498.
- [42] D.D. Macdonald, A. Sun, An electrochemical impedance spectroscopic study of the passive state on Alloy-22, *Electrochim. Acta* 51 (2006) 1767–1779.
- [43] B. Hirschorn, M.E. Orazem, B. Tribollet, V. Vivier, I. Frateur, M. Musiani, Determination of effective capacitance and film thickness from constant-phase-element parameters, *Electrochim. Acta* 55 (2010) 6218–6227.
- [44] D. Wallinder, J. Pan, C. Leygraf, A. Delblanc-Bauer, Eis and XPS study of surface modification of 316LVM stainless steel after passivation, *Corros. Sci.* 41 (1998) 275–289.
- [45] N.E. Hakiki, M. Da Cunha Belo, A.M.P. Simões, M.G.S. Ferreira, Semiconducting properties of passive films formed on stainless steels: influence of the alloying elements, *J. Electrochem. Soc.* 145 (1998) 3821–3829.
- [46] J. Williamson, O.B. Isgor, The effect of simulated concrete pore solution composition and chlorides on the electronic properties of passive films on carbon steel rebar, *Corros. Sci.* 106 (2016) 82–95.
- [47] H. Luo, X. Wang, C. Dong, K. Xiao, X. Li, Effect of cold deformation on the corrosion behaviour of UNS S31803 duplex stainless steel in simulated concrete pore solution, *Corros. Sci.* 124 (2017) 178–192.
- [48] H. Luo, C.F. Dong, K. Xiao, X.G. Li, Characterization of passive film on 2205 duplex stainless steel in sodium thiosulphate solution, *Appl. Surf. Sci.* 258 (2011) 631–639.
- [49] L.A.S. Ries, M. Da Cunha Belo, M.G.S. Ferreira, I.L. Muller, Chemical composition and electronic structure of passive films formed on alloy 600 in acidic solution, *Corros. Sci.* 50 (2008) 676–686.
- [50] L. Hamadou, A. Kadri, N. Benbrahim, Impedance investigation of thermally formed oxide films on AISI 304L stainless steel, *Corros. Sci.* 52 (2010) 859–864.
- [51] K. Tanahashi, N. Inoue, Non-equilibrium thermodynamic analysis on the behaviour of point defects in growing silicon crystals: effects of stress, *J. Mater. Sci. -Mater. El* 10 (1999) 359–363.
- [52] A. Fattah-Alhosseini, F. Soltani, F. Shirasalimi, B. Ezadi, N. Attarzadeh, The semiconducting properties of passive films formed on AISI 316 L and AISI 321 stainless steels: a test of the point defect model (PDM)[J], *Corros. Sci.* 53 (2011) 3186–3192.
- [53] C. Baruffaldi, U. Casellato, S. Cattarin, M. Musiani, B. Tribollet, B. Vercelli, Characterisation of the surface films formed on Nb during electrodissolution in aqueous alkali, *Electrochim. Acta* 47 (2003) 2989–2997.
- [54] B. Ter-Ovanessian, C. Alemany-Dumont, B. Normand, Electronic and transport properties of passive films grown on different Ni-Cr binary alloys in relation to the pitting susceptibility, *Electrochim. Acta* 133 (2014) 373–381.
- [55] W.S. Li, J.L. Luo, Electrochemical investigations on formation and pitting susceptibility of passive films on iron and iron-based alloys, *Int. J. Electrochem. Sci.* 2 (2007) 627–665.
- [56] C. Olsson, The influence of nitrogen and molybdenum on passive films formed on the austenoferritic stainless steel 2205 studied by AES and XPS, *Corros. Sci.* 37 (1995) 467–479.
- [57] P. Keller, H. Strehblow, XPS investigations of electrochemically formed passive layers on Fe/Cr-alloys in 0.5 M H<sub>2</sub>SO<sub>4</sub>, *Corros. Sci.* 46 (2004) 1939–1952.
- [58] M. Zhu, Q. Zhang, Y.F. Yuan, S.Y. Guo, J. Pan, Passivation behavior of 2507 super duplex stainless steel in simulated concrete pore solution, *J. Mater. Eng. Perform.* 29 (2020) 3141–3151.
- [59] M. Seo, N. Sato, Differential composition profiles of passive films on inconel 600 and incoloy 800 alloys, *Corrosio* 36 (1980) 334–339.
- [60] L. Guan, Y. Li, G. Wang, Y. Zhang, L. Zhang, pH dependent passivation behavior of niobium in acid fluoride-containing solutions, *Electrochim. Acta* 285 (2018) 172–184.
- [61] D.D. Macdonald, The history of the point defect model for the passive state: a brief review of film growth aspects, *Electrochim. Acta* 56 (2011) 1761–1772.
- [62] G.T. Burstein, P.I. Marshall, The coupled kinetics of film growth and dissolution of stainless steel repassivating in acid solutions, *Corros. Sci.* 24 (1984) 449–462.
- [63] S.J. Ahn, H.S. Kwon, Effects of solution temperature on electronic properties of passive film formed on Fe in pH 8.5 borate buffer solution, *Electrochim. Acta* 49 (2004) 3347–3353.
- [64] H. Luo, H. Su, C. Dong, X. Li, Passivation and electrochemical behavior of 316L stainless steel in chlorinated simulated concrete pore solution, *Appl. Surf. Sci.* 400 (2017) 38–48.
- [65] N. Sato, Toward a more fundamental understanding of corrosion processes, *Corrosion* 45 (1989) 354–368.